Fungal Spore Sensor Design Using Magnetic Resonance Force Microscopy

A Thesis Submitted
to the College of Graduate Studies and Research
in Partial Fulfillment of the Requirements
for the Degree of Master of Science
in the Department of Electrical and Computer Engineering
University of Saskatchewan

by

Michael A. Rowe

Saskatoon, Saskatchewan, Canada

Permission to Use

In presenting this thesis in partial fulfillment of the requirements for a Postgraduate degree from the University of Saskatchewan, it is agreed that the Libraries of this University may make it freely available for inspection. Permission for copying of this thesis in any manner, in whole or in part, for scholarly purposes may be granted by the professors who supervised this thesis work or, in their absence, by the Head of the Department of Electrical and Computer Engineering or the Dean of the College of Graduate Studies and Research at the University of Saskatchewan. Any copying, publication, or use of this thesis, or parts thereof, for financial gain without the written permission of the author is strictly prohibited. Proper recognition shall be given to the author and to the University of Saskatchewan in any scholarly use which may be made of any material in this thesis.

Request for permission to copy or to make any other use of material in this thesis in whole or in part should be addressed to:

Head of the Department of Electrical and Computer Engineering
57 Campus Drive
University of Saskatchewan
Saskatoon, Saskatchewan, Canada
S7N 5A9

Acknowledgments

There are a number of individuals whose support and encouragement during my graduate career that have made this work possible. First and foremost, I would like to thank Professor Anh Dinh for accepting me as his M.Sc student. It was through his guidance, leadership and support that I was successfully able to complete the sensor design considerations. I must also thank Artur Sowa for explaining some of the mathematical concepts necessary for this project and for access to the Mesoborg cluster, which kept my MATLAB simulation times to a bearable 24 hours or less. I'd also like to thank Sabien Banniza and Randy Kutcher from the Department of Agriculture who gave me valuable advice in regards to mold spores and monoclonal antibodies. I would also like to thank Van Dang at the NRC Nuclear Magnetic Resonance Lab for doing the solid state NMR experiments on the Botrytis Cinerea spore sample and for allowing me to bounce a few ideas off of him in regards to Nuclear Magnetic Resonance.

This work wouldn't be possible without the support family and friends who supported my decision to return to my studies. They were there to bounce ideas off of, provide much needed distractions, and generally help keep me motivated throughout my studies. Finally, I'd also like to thank my fiance Kimberly Porter who encouraged me to enrol in the M.Sc. program at the University of Saskatchewan and was always there to keep me level headed when results didn't turn out the way I had expected or when my simulations failed after running for over a week at a time.

Abstract

This work explores some of the considerations for the design and operation of a fungal spore sensor using Magnetic Resonance Force Microscopy (MRFM). This work starts by introducing the physics, components and theory of operation which make MRFM a favourable method for detecting the presence of fungal spores, which have physical dimensions in the range of a few microns to a few hundred microns.

MATLAB was used to simulate changes in the dipole magnetic force which acts between a mold spore and a MEMS cantilever beam during a MRFM experiment. The dimensions, characteristics and response of the cantilever beam is estimated using MATLAB and refined with multiple simulations in COMSOL Multiphysics. The results are two cantilever models, one made using silicon and the other silicon nitride, have approximate quality factors of 30, spring constants around 80×10^{-6} N/m and resonance frequencies close to 10 kHz.

This work also discusses the proposed manufacturing process and considerations for the MEMS cantilever structure and the additional components of the intended prototype sensor. A sequence of operation for the initial calibration and typical operation of the spore sensor is also included in this work. The fungal spore itself is adhered within the sensing range of the sensor by using an antibody selectively chosen to bind with the targeted spore. This work concentrates on the detection of the Botryris cinerea fungal spore, however the results from this work can be easily expanded on to detect additional fungal spores by changing the monoclonal antibody used to target the other spore types.

Table of Contents

List of Tables

List of Figures

List of Abbreviations

AFM	Atomic Force Microscopy
DNA	Deoxyribonucleic Acid
FM	Ferromagnetic
KOH	Potassium Hydroxide
LLDPE	Linear Low-Density Polyethylene
LPCVD	Low-Pressure Chemical Vapour Deposition
MEMS	Micro ElectroMechanical Systems
MIBK/IPA	Methylisobutylketone/Isopropanol
MRFM	Magnetic Resonance Force Microscopy
MRI	Magnetic Resonance Imaging
NMR	Nuclear Magnetic Resonance
PDA	Potato Dextrose Agar
PMMA	Polymethylmethacrylate
ppm	Parts per Million
RF	Radio Frequency
SNR	Signal to Noise Ratio

1. Introduction

Fungal infection in crops is a growing concern for many farmers across the globe. There are millions of different genus of fungi, some of which are capable of causing billions of dollars in damages to agricultural crops worldwide. Fungal infections are spread between infected and healthy host plants by the distribution of fungal spores via water flow, wind currents and insects. The traditional method of checking plants for fungal pathogens is through a visual check of the crop leaves, stocks and kernels for the signs of disease. Once the presence of an infection has been identified a broad spectrum fungicide is used to treat the fungus in the infected fields, typically without knowing the family or genus of the fungus. Usually by the time a fungal infection has been identified and sprayed, the fungus has already caused significant damage to the infected plants which results in a lower crop yield and overall poorer quality. In more advanced growing facilities such as greenhouses and government growing operations, a number of precautions are used to prevent fungal infections such as high quality water and air filters.

Current methods for detecting the presence of mold spores involves using spore traps to capture airborne spores and collect them on a tape or filter which is then inspected manually by a technician using a microscope or by using DNA-based identification methods on the collected sample [1]. Typically the tape or filter goes through a period of incubation before the identification process, which encourages the mold spore to grow vegetative stocks called conidiophores, which aids in the identification of the fungi species. While this approach in spore identification is an attempt to be proactive, the process for incubation of the filters and the manual inspection can be rather time consuming which introduces delays between the time the sample was initially acquired and the time the fungus is positively identified. This

delay grants the mold spores in the field more time to reach maturity and infect additional plants. In order to combat the increased fungal presence more fungicide needs to be used to treat the infected crop. Fungicides used to treat fungal infections can have unwanted effects on other beneficial organisms, or build up chemical residue in the soil or the food chain [2].

It is desirable to design a sensor which can replace the tape or filter within a spore trap to detect the presence of mold spores without the need for the transportation, incubation and visual inspection of a traditional spore trap filter. Using mechanical means for the detection of mold spores can be quite challenging, as the size of the spore is extremely small, ranging from a few microns to a hundreds of microns on a side. Magnetic resonance force microscopy (MRFM) is a technique which combines the high resolution scans of magnetic resonance imaging (MRI) and the force sensitivities of Atomic Force Microscopy (AFM) to detect the minuscule changes in the net magnetization of a sample. In close proximity and the right environmental conditions, such as under a high vacuum and near $0°K$, MRFM experiments have been able to detect the spin of a single electron [3–5]. In this work, mathematical models and finite element analysis are used to investigate the feasibility of a sensor utilizing MRFM techniques for the detection of a single mold spore.

This work will focus on the detection of the fungus Botrytis Cinerea, which infects a variety of host plants and is the cause of grey mold on a number of fruits including tomatoes, grapes and strawberries both pre- and post- harvest. The botrytis spore was chosen because

(a)

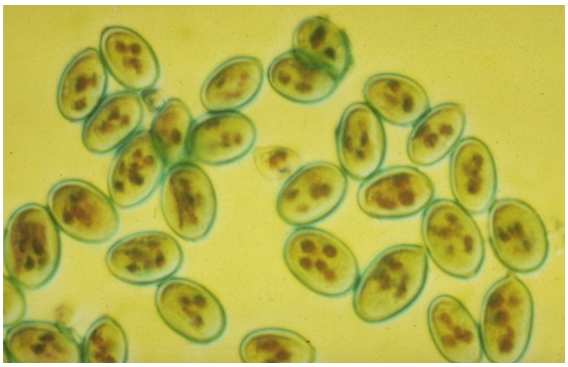

(b)

Figure 1.1: Botrytis cinerea **a.** growth on a strawberry and **b.** individual spores.

it is a common infection amongst fruit and vegetable farmers, and because the monoclonal antibody which acts as an binding layer between the sensor and the spore is readily available. While this works focus on the detection of the botrytis spore, the techniques used in the development of the sensor can be expanded on for the detection of other fungal spores which can be bonded to a monoclonal antibody.

1.1 Motivation

A sensor capable of detecting the presence of mold spores such as botrytis cinerea has applications in many industries outside of the agriculture sector. One possible application is to place the proposed mold spore sensors within the compartments of a refrigerator for the detection of fungi growth on produce, cheese or dairy products. Early detection of mold in refrigerators can help prevent the fungus from spreading from infected products to healthy, non-infected food.

Another application of such a sensor is in the potash industry. Rail cars and ships used to transport potash to Australia and New Zealand need to be 100% free of the fungus Tilletia indica. Wheat crops infected with tilletia indica develop karnal bunt disease which is profoundly difficult to detect on crops, but results in a foul taste and smell when flour is made with infected kernels. Fertilizers such as potash suspected of being in contact with tilletia indica are not allowed to dock in Australian ports, which can result in hundreds of tonnes of potash being turned away [6]. Fungal spore sensors at different stages of the potash storage and transportation process can alert staff if signs of the fungus are found either before containers are filled, or if the product gets contaminated during the shipping process.

Air handling units in office buildings and schools collect and distribute thousands of litres of air a day and provide a great pathway to distribute airborne spores throughout a building. Air samplers capable of detecting mold spores can be placed in a buildings ductwork and be used to detect the spores of fungus such as Stachybotrys chartarum or Stachybotrys chlorohalonata which can indicate the presence of toxic black mold growth in the building. Numerous other fungal spores distributed throughout a building may not be toxic but can

be a cause of many allergic reactions or illnesses in building occupants [7].

1.2 Research Objectives

The following objectives are defined for this thesis study:

Objective 1: *To estimate the dipole magnetic force which acts between the ferromagnetic particle attached to a cantilever beam in the MRFM setup and a single botrytis cinerea spore, and determine at what RF frequency the magnetic force is maximum.*

The method used to accomplish this objective is to determine the mathematical systems involved in a MRFM experiment and model those systems using a MATLAB script. A sweep of the applied RF frequency is used to determine at what frequency the magnetic force is maximized.

Objective 2: *To determine the required cantilever beam properties such that the MRFM setup can detected the minute changes in the magnetic field, and determine the cantilever dimensions which result in the smallest spring constant while maintaining the ideal mechanical resonance frequency of 10 kHz.*

The procedure used to achieve this objective involves estimating the dimensions of the cantilever beam and the resulting properties using a MATLAB script. The results of the script are then verified and adjusted using COMSOL Multiphysics.

Objective 3: *To estimate the response of the cantilever beam during a MRFM experiment and determine the amount of time required for the cantilever oscillations due to MRFM to be distinguishable from thermal oscillations.*

The method used to achieve this objective involves applying a harmonic load to the cantilever beam in COMSOL multiphysics and measuring the time required for the cantilever oscillations to double the amplitude of the thermal vibrations of the cantilever beam.

Overall, the general methodology for conducting this research is to determine if a MEMS device can accurately detect the presence of a botrytis cinerea mold spore by using multiple simulations. The results of this study can be expanded on to develop a prototype of the proposed mold spore sensor.

1.3 Thesis Organization

The remainder of this thesis is organized into four additional chapters. Chapter 2 will provide background information on nuclear magnetic resonance and the different components of magnetic resonance force microscopy. Chapter 2 will also introduce the botrytis cinerea mold spore, its associated monoclonal antibody, and the results of solid state NMR experiments done on the spore. Chapter 3 discusses the MATLAB script and COMSOL simulations used to estimate the dimensions and characteristics of the MEMS cantilever used in the proposed sensor. The MATLAB script used to estimate the force resulting from a magnetic resonance force microscopy experiment using a homogeneous sample is reviewed. Chapter 4 examines the design considerations and manufacturing process for the proposed sensor and discusses the sequence of operation for the sensor. Chapter 5 reviews the overall structure and discusses future work and consideration for construction and verification of the sensor operation.

2. Background

This chapter will introduce nuclear magnetic resonance and review the physics involved in the operation of a typical experiment. The differences between solution and solid state nuclear magnetic resonance experiments will be discussed. These concepts are expanded upon as an introduction to magnetic resonance force microscopy and a breakdown of the roles each component plays in experiments including the MEMS cantilever beam, RF coil and permanent magnet. The botrytis cinerea spore and the monoclonal antibodies BC-12.CA4 are also discussed in detail and the results of a solid state NMR on a large number of spores are reviewed.

2.1 Nuclear Magnetic Resonance

Nuclear Magnetic Resonance (NMR) is a technique which uses a large magnetic field and a RF signal to manipulate the nuclear magnetic moments of individual nuclei within a sample to discern the types of nuclei present and their proportions within the sample. The NMR effects arises due to the property called nuclear spin (I), which is dependent on the number of proton and neutrons within the nucleus of an atom. The nuclear spin is calculated by the vector addition of the quantum spin numbers for individual proton and neutron, each with a value of $\frac{1}{2}$, with the restriction that proton spins can only cancel out other proton spins, and likewise for neutrons. A nuclei with an odd number of protons or neutrons (but not both) is referred to as a dipolar nuclei and has a nuclear spin of $I = \pm\frac{1}{2}$. The nuclear magnetic moment (μ) associated with a given nuclei is given by:

$$\mu = \gamma I\hbar \quad \left[\frac{A}{m^2}\right] \tag{2.1}$$

where $\hbar$ is the reduced Planck's constant (1.054589×10^{-34}Js). The gyromagnetic ratio, γ, is the proportionality constant which relates the magnetic moment of an isotope to its angular momentum [8]. The natural abundance of an isotope is the probability that an isotope of a given element occurs naturally, a high natural abundance is a desirable trait for a good NMR signal. The natural abundance and gyromagnetic ratios of select isotopes with a $\pm\frac{1}{2}$ spin are listed in Table 2.1 [9].

Table 2.1: Gyromagnetic ratios and natural abundance of select nuclei used in MRI

Isotope	Gyromagnetic Ratio $(\gamma/10^7)\frac{rad}{Ts}$	Natural Abundance (%)
^{1}H	26.7519	99.985
^{13}C	6.7283	1.108
^{19}F	25.1815	100
^{19}P	10.8394	100

In the absence of an external magnetic field, the magnetic moments of the nuclei within a sample have a random orientation, resulting in the sample having no net magnetization. When the same sample is placed within a magnetic field of magnitude B_{ext}, which acts in the positive z direction, a torque acts upon the magnetic moments within the sample and results in a circular precession of the individual magnetic moment about the direction of B_{ext}. This rate of precession is referred to as the Larmor Frequency, ν_0, and is proportional to the applied magnetic field strength and the gyromagnetic ratio of the nuclei, as given in Eqn. 2.2.

$$\nu_0 = \frac{\gamma B_{ext}}{2\pi} \quad [\text{Hz}] \tag{2.2}$$

Quantum theory limits the number of orientations nuclei with a $\pm\frac{1}{2}$ spin to two possible orientations [9]. Nuclei which have their magnetic moments precession in the same direction as the external magnetic field results in a lower energy α state, whereas the nuclei which have magnetic moments precessing in the opposite direction results in a higher energy β state. The energy of a given state is given in Eqn. 2.3. Since the value of I is limited to $\pm\frac{1}{2}$

the energy gap resulting from the Zeeman effect can be calculated using Eqn. 2.4. Figure 2.1 shows how the energy levels of the α and β states change as the external magnetic field, B_{ext}, increases.

$$E = -\gamma\hbar I B_{ext} \quad [\text{eV}] \tag{2.3}$$

$$E_{I=+\frac{1}{2}} = \frac{-\gamma\hbar B_{ext}}{2}$$

$$E_{I=-\frac{1}{2}} = \frac{\gamma\hbar B_{ext}}{2}$$

$$\Delta E = E_{I=-\frac{1}{2}} - E_{I=+\frac{1}{2}}$$

$$\Delta E = \gamma\hbar B_{ext} \quad [\text{eV}] \tag{2.4}$$

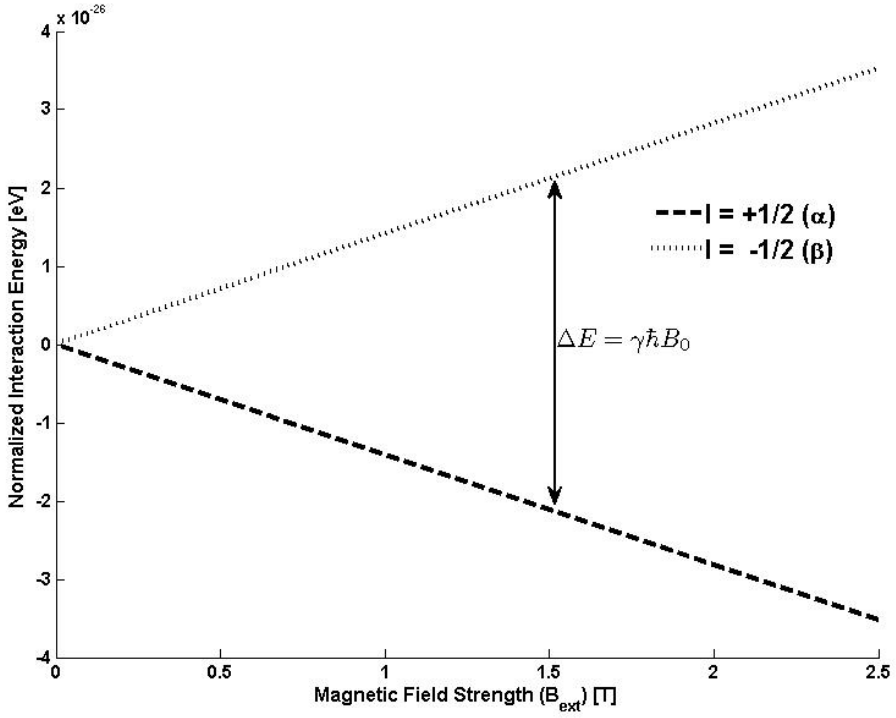

Figure 2.1: The relationship of the energy level of $\pm\frac{1}{2}$ spins as the external magnetic field increases.

If its assume that the test sample is in thermal equilibrium, the ratio of the number of spins in each state as governed by the Boltzmann distribution given in Eqn. 2.5a, where k_b is the Boltzmann's constant ($1.3806503 \times 10^{-23}$Js), T is the temperature in °K, and $\frac{N_\beta}{N_\alpha}$ is the ratio of the number of spins in the β state and the number of spins in the α state. At

temperatures above 50 °K, the ratio of spins in the α and β states is extremely close to 1:1, with the α state having a slightly larger concentration of spins then the β state.

$$\frac{N_\beta}{N_\alpha} = e^{\frac{\gamma\hbar B_{ext}}{k_b T_0}} \tag{2.5a}$$

$$= 1 - \frac{\gamma\hbar B_{ext}}{k_b T_0} \quad \text{when } \gamma\hbar B_{ext} < k_b T_0 \tag{2.5b}$$

When a sample with a higher concentration of α spins and is bombarded by a low power RF field oscillating at the Larmor frequency (ν_0) the spins in the α state absorbs the RF energy boosting them into the higher energy β state. This transition results in the magnetic moment of the spin to change its direction to points away from B_{ext}; this phenomenon is known as a spin flip. This absorption of energy will continue to occur until the sample is removed from the RF field, or the sample becomes saturated such that $N_\alpha = N_\beta$. Once the RF field is removed from the sample, the nuclei affected by the RF pulse will relax back to the initial Boltzmann distribution. There are two basic mechanisms for relaxation [9].

a. Spin-Lattice Relaxation *(T_1 Relaxation)* occurs when a nuclei in the β state transfers its energy to other atoms or ions within the lattice or backbone of the sample. As the energized β state nuclei transitions back into the α state, the nuclei undergoes another spin flip as it releases its energy and results in a small RF pulse being released. This RF pulse has an equivalent energy as the energy gap between the two states.

b. Spin-Spin Relaxation *(T_2 Relaxation)* occurs when a nuclei in the β state transfers its energy upon a nuclei in the α state. In this case, two spin flips occur simultaneously and results in no net change in energy or state population of the sample.

The RF pulse released by the Spin-Lattice relaxation is the fundamental signal measured in nuclear magnetic resonance and can be measured using a receiving RF antenna. In a laboratory environment with an external magnet capable of 2 Tesla or more, the RF signals released from the sample tend to occur in the MHz range. A typical NMR experiment setup consists of a transmit/receiving antenna pair as well as permanent and sweeping magnets, as shown in Figure 2.2. For this setup, the external magnetic field is swept using sweep

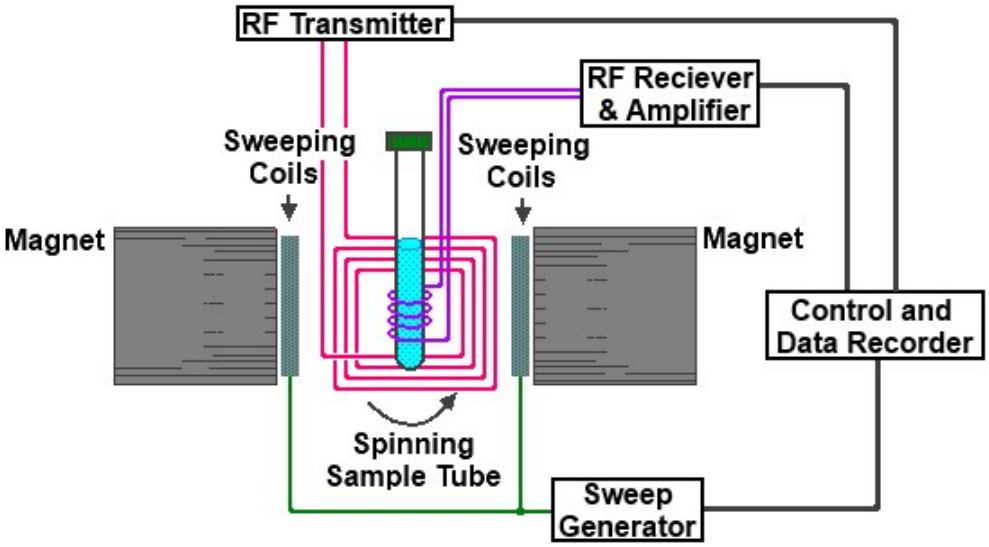

Figure 2.2: Typical NMR experiment setup [10]

coils while the transmitted RF frequency remains constant. Once a signal has been received by the Rx antenna, it is typically passed through a Fourier transform which results in a spectrum similar to the one shown in Figure 2.3.

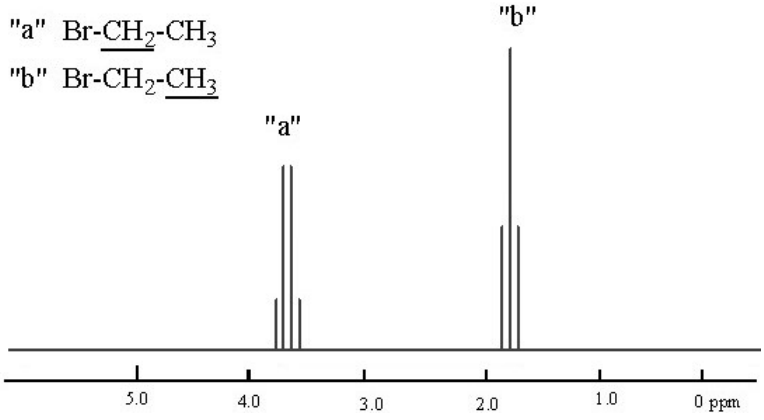

Figure 2.3: H^1 NMR spectrum of ethyl bromide [11].

The spectrum shown in Figure 2.3 is the NMR spectrum for ethyl bromide and introduces the concept of chemical shift (δ) within a sample. The spins which react in a NMR experiment are influenced by the magnetic shielding of nearby atoms and their electrons. In the case of ethyl bromide, the bromine atom has a relatively high electro-negativity compared to the hydrogen and carbon atoms in which it shares the molecule. The higher electronegative Br

attracts the electrons of the neighboring atoms towards it, this results in a deshielding effect which exposes the CH_2 molecule labelled "a" to the RF pulse slightly more than the CH_3 molecule labelled "b". This deshielding effect introduces minuscule differences in the local magnetic fields of the CH_2 and CH_3 resulting in offsets in the larmor frequency between the two parts of the molecule. The offset between the two larmor frequencies is measured in parts per million (ppm) and can be estimated using Eqn. 2.6. The frequency shift in magnetic resonance has a range of a few Hz compared to the operating frequency of the NMR spectrometer, which tends to be in the few hundred MHz range [12] which is why the chemical shift has the units of ppm. The ppm measurements normalize the NMR spectrum to the operating frequency of the MRI used, allowing for the same compound experimented on using different spectrometers having comparable spectra. The x-axis of NMR spectra shows the frequency difference between the peaks of the spectrum in ppm and the y-axis represents the strength of the measured RF signal (unit less). By comparing the magnitude of the peaks of the spectrum and the frequencies differences between those peaks, its possible to determine the chemical composition of the sample under test.

$$\delta = \frac{\upsilon - \upsilon_{ref}}{\upsilon_{ref}} \quad [ppm] \tag{2.6}$$

Magnetic resonance experiments have slightly different approach when performed on solid samples. Most solid NMR experiments are performed on powdered substances which results in random spin orientations within the sample. This random orientation causes a directional dependence in the chemical shift of the sample which needs to be compensated for otherwise the solid NMR spectrum will have extremely broad peaks, which can make determining the chemical structure of the sample a tedious and troublesome task. In order to remove the directional dependence of the sample during testing, the z-axis of the sample is offset by 54.74° and sample is rotated at a high speed. The angle 54.75° is referred to in solid NMR as the magic angle and helps average the directional dependence of the solid or powdered samples resulting in the narrowing the peaks in the solid NMR spectrum [13]. Figure 2.4 gives an example of the differences in spectra between the solution based NMR and a solid state NMR, in this case ^{13}C spectrum of linear low-density polyethylene (LLDPE) [14].

One of the disadvantages of standard nuclear magnetic resonance is that the magnitude

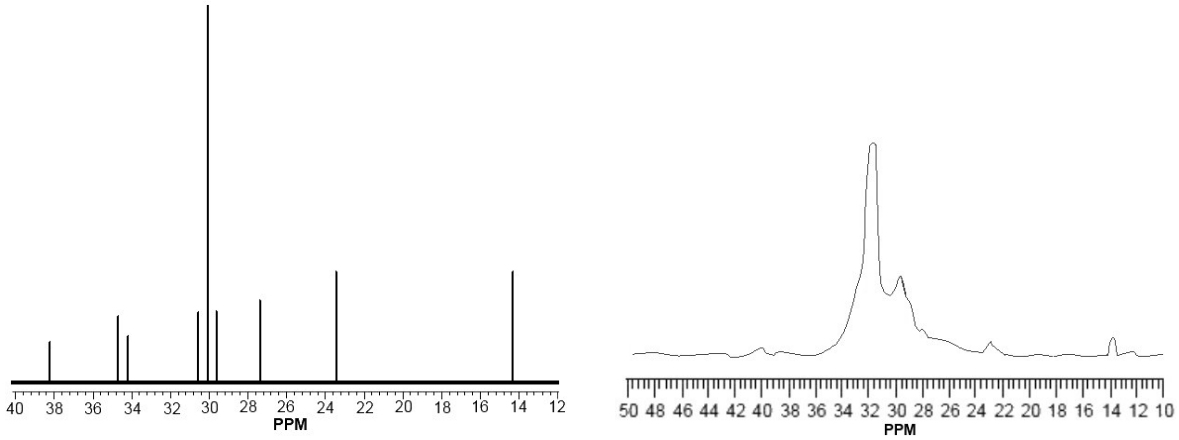

(a) (b)

Figure 2.4: A comparison of ^{13}C spectrum for linear low-density polyethylene from: **a.** solution NMR and **b.** solid state NMR [11]

of the RF pulse emitted by the sample is dependent on the number of spin-flips which occur within the sample. The number of spins in a sample is limited to the volume of the sample; therefore the Signal-to-Noise Ratio (SNR) of the received signal is directly proportional to the volume of the sample. Since the final goal of this sensor design is to detect the presence of a single mold spore which has the dimensions of a few micron in comparison to the distance to the RC coil in a NMR spectrometer, which can be up to a centimeter away from the sample, the probability of obtaining a detectable RF signal from a single mold spore is extremely low.

Due to the complex nature of the atomic arrangement within molecules, Shoolery's rule was devised to be used to estimate the chemical shift for any CH_2-X-Y or $CH-X-Y-Z$ systems. Section 2.1.1 introduces the concepts behind Shoolery's rules and contains a table of calculated chemical shift contributions, a few examples of chemical shift calculations and their comparison to experimental values.

2.1.1 Shoolery's Rules

As mentioned previously, the chemical shift observed in NMR experiments are caused by localized magnetic shielding and deshielding due to other atoms in the system and their

electro-negativity. The chemical shift can be estimated based on the known values observed in methane ($\delta = 0.23ppm$) and summing the contributions of adjacent molecules to predict the final chemical shift for a CH group. These estimations provide good results for CH_2 groups, but are less accurate for CH groups; CH_3 groups can be estimated by substituting in $H - CH_2 - X$. The equation for estimating the chemical shift using Shoolery's rule is given in Eqn. 2.7 and a list of chemical shift contributions is given in Table 2.2 [9].

$$\delta = 0.23 + \sum \text{Contributions} \tag{2.7}$$

Table 2.2: Additive Contributions to the Chemical Shifts of CH and CH_2 Groups

Group	Contribution	Group	Contribution
H	0.17	$CO\mathbf{R}$	1.70
CH_3	0.47	I	1.82
$CH_2\mathbf{R}$	0.67	Ph	1.85
CF_3	1.14	Br	2.33
$C = C$	1.32	$O\mathbf{R}$	2.36
$C \equiv C\mathbf{R}$	1.44	Cl	2.53
$CO_2\mathbf{R}$	1.55	OH	2.56
$N\boldsymbol{R}_2$	1.57	$O.CO.\mathbf{R}$	3.13
$CON\boldsymbol{R}_2$	1.59	$0.Ph$	3.33
$S\boldsymbol{R}$	1.64	F	3.60
CN	1.70	$\mathbf{R}CONH$	2.36

The following examples show how to use Shoolery's rules to estimate the spectral peaks for simple compounds before comparing the location of the estimated peaks to the spectral peaks observed from NMR experimental data.

Example 1

For the compound CH_3CH_2Cl the ^{1}H chemical shifts can be estimated as follows:

$\underline{CH_3}CH_2Cl$ $\qquad \delta = 0.23 + 0.17 + 0.47 = 0.7ppm$

$CH_3\underline{CH_2}Cl$ $\qquad \delta = 0.23 + 0.47 + 2.53 = 3.23ppm$

For the above example, spectral peaks from an NMR experiment are estimated to be around 0.7 ppm and 3.23 ppm. For this compound run in a solution NMR, the experimental peaks are observed at 0.78 ppm and 3.57 ppm.

Example 2

For the compound CH_2Cl_2 the ^{1}H chemical shift can be estimated as follows: $\underline{CH_2}Cl_2$

$\delta = 0.23 + (2)(2.53) = 5.29ppm$

For this example, a spectral peak from an NMR experiment is estimated to be around 5.29 ppm. The NMR experimental peak is located at 5.32 ppm.

2.2 Magnetic Resonance Force Microscopy

Magnetic Resonance Force Microscopy (MRFM) is a technique which incorporates aspects of Atomic Force Microscopy (AFM) with traditional nuclear magnetic resonances to increase the SNR of samples with a small volume. This technique uses a Micro Electro-Mechanical System (MEMS) cantilever with small spring constants to measure the net dipole magnetic force that acts between the sample under test and a ferromagnetic (FM) particle attached to the end of the cantilever. The dimensions of MEMS devices are in the range of a few nm to a few mm which gives MRFM an advantage over traditional NMR in that the SNR of the received signal is higher for small sample volumes, such as the size of a mold spore [15]. Figure 2.5 shows an example of a typical MRFM setup, although multiple variations have

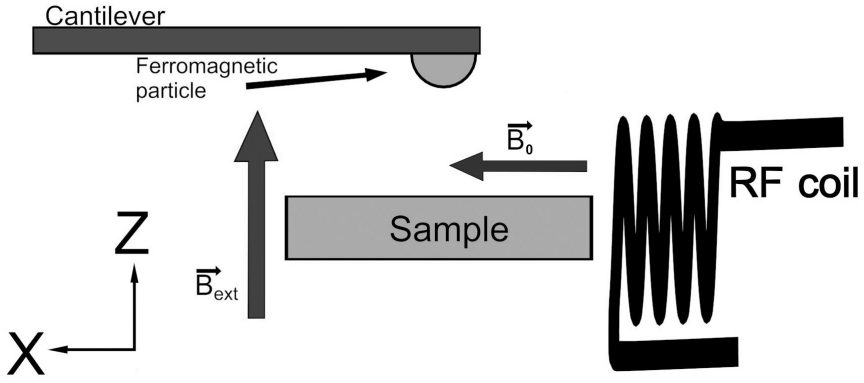

Figure 2.5: Typical MRFM experiment setup [15].

been designed and tested, the principle of the experiment remains the same. In a typical MRFM experiment, a ferromagnetic (FM) particle is suspended by the free end of a MEMS cantilever beam. A permanent magnet is used to provide a homogeneous external magnetic field, B_{ext}, perpendicular to the plane of the cantilever. The sample is located between the permanent magnet and the ferromagnetic particle. An RF coil is positioned such that the magnetic field of the RF frequency B_0, is perpendicular to B_{ext}. For simplicity the orientation of B_{ext} will be define in the positive z-direction and the RF pulse B_0 acts in the positive x-direction. As with the traditional NMR theory, the permanent magnet induces Zeeman splitting in the sample and the energy absorbed from RF pulse induces spin flips from the α to β state. Once the RF pulse is turned off and T1 relaxation occurs the MEMS cantilever oscillates as the net magnetization of the sample varies during the nuclei transition from the β state to the α state. In order for the MRFM mechanism to successfully measure such small magnetic variations, the cantilever beam must be designed with a low spring constant for the highest sensitivity.

2.2.1 MEMS Cantilever Beam

The motion of a MEMS cantilever beam can be modeled as a second order damped spring as given by Eqn. 2.8 where F_0 is a harmonic load applied to the cantilever beam at the frequency α. The values of m, k and c are the mass, spring constant and damping factor of the cantilever beam and can be estimated using Eqn. 2.9, 2.10, and 2.11 respectively. The estimated resonance frequency of the cantilever beam is given by Eqn. 2.12, where E_c and ρ_c are the Young's modulus and density of the cantilever material respectively and λ_n is the flexural mode identifier constant ($\lambda_1 = 1.875$). The cantilever length l_c, width w_c, and thickness t_c all play an important role in the harmonic oscillations of the mass-spring system. The dimensions of the cantilever beam also have an effect on a number of different damping coefficients.

$$m\ddot{x} + c\dot{x} + kx = \quad F_0 \sin(\alpha t) \tag{2.8}$$

$$m = \quad \rho l_c w_c t_c \qquad [kg] \tag{2.9}$$

$$k = \quad \frac{E w_c t_c^3}{4 l_c^3} \qquad \left[\frac{N}{m}\right] \tag{2.10}$$

$$c = \quad \frac{1}{2Q} \qquad \left[\frac{N}{m^2}\right] \tag{2.11}$$

$$\omega_c = \quad \frac{\lambda_n^2}{\sqrt{12}} \frac{t_c}{l_c^2} \sqrt{\left(\frac{E_c}{\rho_c}\right)} \qquad \left[\frac{rads}{s}\right] \tag{2.12}$$

The quality factor (Q) of a cantilever beam is the ratio of the mechanical energy stored in the cantilever versus the energy dissipated per cycle [16]. A high Q results in better frequency stability and sensing resolution from the cantilever as more energy is stored in the beam. Energy loss can occur in the cantilever beam due to multiple damping mechanisms related to the operating environment of the cantilever, material the beam is manufactured from and geometry of the beam. The overall quality of the cantilever beam can be calculated from the quality factors of individual damping phenomena using Eqn. 2.13. Examples of different damping mechanisms include squeeze film air-damping, Stoke's damping, thermoelastic damping and clamp damping.

$$Q_{tot} = \quad \left(\frac{1}{Q_1} + \frac{1}{Q_2} + ...\right)^{-1} \tag{2.13}$$

Squeeze-film damping is caused when a cantilever is oscillating near a surface parallel to the length of the cantilever beam. As the cantilever oscillates it collides with the molecules in the air, passing on some of the cantilever energy to the air molecules and forcing the molecules to be pushed out from between the cantilever beam and the surfaces parallel to it. Stoke's damping describes the drag force that acts upon the lateral motion of the cantilever beam within a gas or fluid [17].

Equations 2.14 and 2.15 can be used to approximate the quality factor due to Stoke's damping and squeeze-film damping respectively, where h_0 is the distance between the cantilever rest position and the surface it is interacting with, M is the molar mass of air (29.96 g/mol) and R is the ideal gas constant (8.3145 $\frac{J}{mol\,^\circ K}$). T_0 and P_0 are the operating tem-

perature ($^\circ K$) and pressure (Pa) of the system. The mean free path of air can be estimated using Eqn. 2.16 where d is the diameter of the air molecule (approximately 39 nm) and the value of the dynamic viscosity of air, η, is interpolated from the values in Table 2.3 [18].

$$Q_{St} = \frac{m}{l_c w_c}\sqrt{\frac{\omega_0 R T_0}{2 P_0 M \eta}} \tag{2.14}$$

$$Q_{Sq} = \frac{(1 + 9638\left(\frac{\lambda}{h_0}\right)^{1.159})\pi^4 h_0^3 t_c * \rho_c \omega_0}{96\eta w_c^2} \tag{2.15}$$

$$\lambda = \frac{k_b T_0}{\sqrt{2}\pi d^2 P_0} \tag{2.16}$$

Table 2.3: Dynamic viscosity of air at given temperatures.

Temperature	$0^\circ C$	$20^\circ C$	$60^\circ C$	$100^\circ C$	
Air	17.08	18.75	20.00	22.00	$\times 10^{-6} N\frac{s}{m^2}$

Additional forms of damping can occur from the interactions of the crystal lattice of the cantilever material. The magnitude of these intrinsic losses can be quite large if the cantilever beam is not designed with this in mind. The support losses occur due to the elastic and acoustic losses that dissipate from the cantilever beam to the support structure. An estimation of the quality factor due to losses from the support structure, Q_{clamp}, is a function of both the cantilever length and thickness, as shown in Eqn. 2.17, where κ is a calculated coefficient having the value of 0.34, 2.17 or 2.081 depending on the study [19].

$$Q_{clamp} = \kappa\left(\frac{l_c}{t_c}\right)^3 \tag{2.17}$$

Thermoelastic damping is another example of intrinsic damping which occurs within the cantilever beam structure. When a beam is oscillating localized expansions and compressions occur within the beam structure. These compression regions result in a localized increase in temperature and the expansion regions result in a localized decrease in temperature (assuming a positive coefficient of thermal expansion) [20]. These changes in temperature within the cantilever structure get dissipated into the surrounding medium resulting in energy loss within the system. The quality factor resulting from the thermoelastic damping of a cantilever beam oscillating at its fundamental frequency is estimated in Eqn. 2.18 where α,

C_p and κ_{th} is the linear thermal expansion coefficient, specific heat capacity and thermal conductivity of the cantilever material [21, 22]. This equation holds for simple cantilever structures, however more complex modeling is required for complicated structures such as laminated or non-symmetrical beams.

$$Q_{TED} = \frac{\rho C_p}{E_c \alpha^2 T_0} \frac{1 + (\omega_c \tau_z^2)}{\omega_c \tau_z} \tag{2.18}$$

$$\tau_z = \frac{\rho C_p t_c^2}{\pi^2 \kappa_{th}} \tag{2.19}$$

For cantilever based sensors a large component of the noise floor is the thermomechanical oscillations. It is for this reason that a high quality factor due to thermoelastic damping is desired. In order for a harmonic force to be distinguishable from the noise floor, the rms amplitude of the driven cantilever oscillations must be greater than the oscillations caused by thermal vibrations in the cantilever beam (Z_{rms}). The rms amplitude of the driven vibrations upon the cantilever can be approximated using Eqn. 2.20 where F is the force which acts on the cantilever and Q is the total quality factor of the cantilever beam given in Eqn. 2.13. The rms amplitude of the thermal vibrations can be estimated using Eqn. 2.21 where Δf is the bandwidth of the measuring device, k_c is the cantilever spring constant, ω_c is the operating frequency of the cantilever and T_0 is the operating temperature ($^\circ K$) of the structure.

$$A_{rms} = \frac{4}{\sqrt{2}\pi} \frac{QF}{k_c} \tag{2.20}$$

$$z_{rms} = \left(\frac{4 k_B T_0 Q \Delta f}{k_c \omega_c} \right)^{1/2} \tag{2.21}$$

Since for MRFM experiments the force which acts upon the cantilever tends to be rather small, the overall deflection of the beam it likely to be equally as small. In order to measure such small deflections of the cantilever beam, a laser interferometer is used to measure the both the cantilever tip amplitude and frequency. The minimum force detected by the cantilever beam can be approximated using Eqn. 2.22 [23].

$$F_{min} = \sqrt{\frac{4 k_b T k}{Q \omega_c}} \quad \left[\frac{N}{\sqrt{Hz}} \right] \tag{2.22}$$

2.2.2 Permanent Magnet

Like traditional MRI experiments, the permanent magnet plays an important role in magnetic resonance force microscopy. The permanent magnet is required to provide a homogeneous magnetic field at the sample location in order to have a uniform distribution of Zeeman splitting within the sample. The magnitude of the external magnetic field, B_{ext} determines the operating frequency of the RF pulse and directly affects the thickness of the resonances slice within the sample. In order to maximize the number of spins in the resonance slice it is desirable to have a permanent magnet which has a large magnetic field.

A typical iron bar magnet can have a magnetic field strength around 0.2 Tesla. In comparison bonded neodymium ($Nd_2Fe_{14}B$) magnets tend to have a magnetic field strength of between 0.6 - 0.7 Tesla, whereas sintered neodymium magnets can have a magnetic field strength between 1.0 - 1.4 Tesla. By aligning the magnetic field of two permanent magnets in the same direction and using a spacer to separate the magnets, a relatively homogeneous magnetic field can be found in the gap between the two magnets.

2.2.3 Ferromagnetic Particle

The ferromagnetic (FM) particle located near the tip of the MEMS cantilever serves two purposes. The first objective is to introduce a magnetic field gradient in the otherwise homogeneous magnetic field as given in Eqn 2.23 where μ_0 is the permeability of free space ($\mu_0 = 4\pi \times 10^{-7} H/M$), r is its radius, and d is the separation between the FM particle and individual nuclear spins [24]. The magnetization of iron is $M = 1.76 \times 10^6 [A/m]$

$$\left|\frac{\partial B_z}{\partial z}\right| = \frac{2\mu_0 M r^3}{(r+d)^4} \quad \left[\frac{T}{m}\right] \tag{2.23}$$

$$F = \nabla(m \cdot B_{ext}) \quad [N] \tag{2.24}$$

$$F_z(t) = m_z(t)\frac{\partial B_z}{\partial z} \quad [N] \tag{2.25}$$

The second purpose of the FM particle is to drive the MEMS cantilever tip by reacting to changes in the net magnetization of the sample under test, resulting in a dipole magnetic force being applied to the FM particle. Equation 2.24 indicates the force F that acts between the FM particle and the sample is related to the magnetic moment of the sample, m, and

the applied magnetic field, B_{ext}. Equation 2.24 also indicates that a gradient is required for a measurable force to be present; hence a large gradient in the magnetic field is desirable. If its assumed that the sample under test is symmetrical about the z-axis then the x and y components of the force cancel out resulting in a symmetrical force about the z-axis. The resulting z-component of the reaction force can be expressed using Eqn. 2.25 [15].

2.2.4 RF Coil

The RF coil of a MRFM experiment is positioned such that the magnetic field from the RF coil, B_0, is perpendicular to the magnetic field of the permanent magnet, B_{ext}, and located as close as possible to the sample undergoing testing. Just like in traditional NMR when the sample is under Zeeman splitting, the energy of the RF field excites the spins in the α state to the β state. The frequency required for this transition is given by Eqn. 2.26 where $\vec{B_d}$ is the dipole magnetic field which acts between the FM particle and the sample spins, given in Eqn. 2.27 for a spin located at the position (x,y,z). Vector $\vec{m}$ is the magnetization of the spin, $\vec{n}$ is the unit vector of the Euclidean distance r and z_c is the z-component of the ferromagnetic particle position.

$$\omega_{rf} = \gamma \left| \vec{B_{ext}} + \vec{B_d} \right| \quad \left[\frac{rad}{s}\right] \tag{2.26}$$

$$\vec{B_d} = \frac{\mu_o}{4\pi} \frac{3(\vec{m}\cdot\vec{n})\vec{n} - \vec{m}}{r^3} \quad [T] \tag{2.27}$$

$$r = \sqrt{x^2 + y^2 + (z - z_c)^2} \quad [m] \tag{2.28}$$

$$\vec{n} = (\frac{x}{r}, \frac{y}{r}, \frac{z - z_c}{r}) \tag{2.29}$$

For a typical MRFM experiment the RF field is generated using a conventional 2-turn copper wire coil with a radius of a few centimeters and is located approximately 2mm from the cantilever tip. Due to the proximity of the permanent magnet and optical sensor to the cantilever, the center of RF coil usually needs to be displaced from the center of the sample and cantilever tip, where the applied magnetic field is maximum. Z. Zhang et al [25] proposed the modified Alderman-Grant coil design shown in Figure 2.6. This design was machined from a solid copper rod to form a 2 turn coil which has a thickness of 0.4mm, a length of 3mm and a diameter of 3mm. The main advantage of this coil design is that it is possible to locate

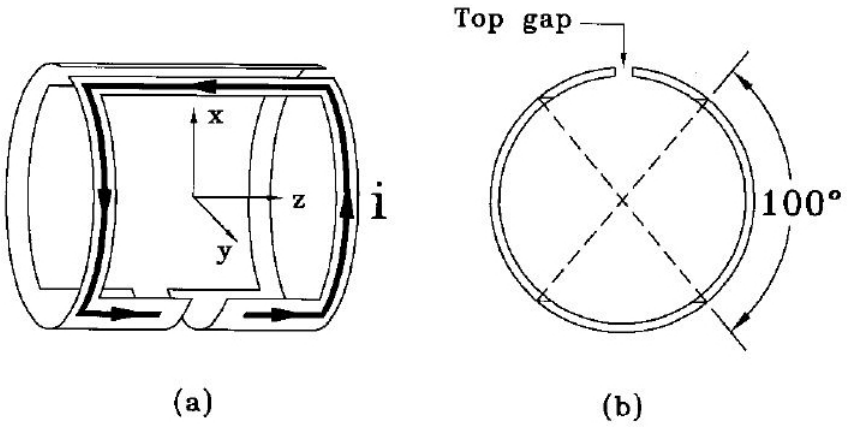

Figure 2.6: Modified Alderman-Grant coil proposed by Zhang [25] **a.** side and **b.** front profile

the cantilever and sample at the center of the coil, where the coil magnetic field strength is maximum. The gaps located at the top and bottom of this coil allow the cantilever to be accessible to both the optical cable of the laser interferometer and the permanent bar magnet. Both the simple copper wire coil and the modified Alderman-Grant coil designs are viable options for the proposed sensor.

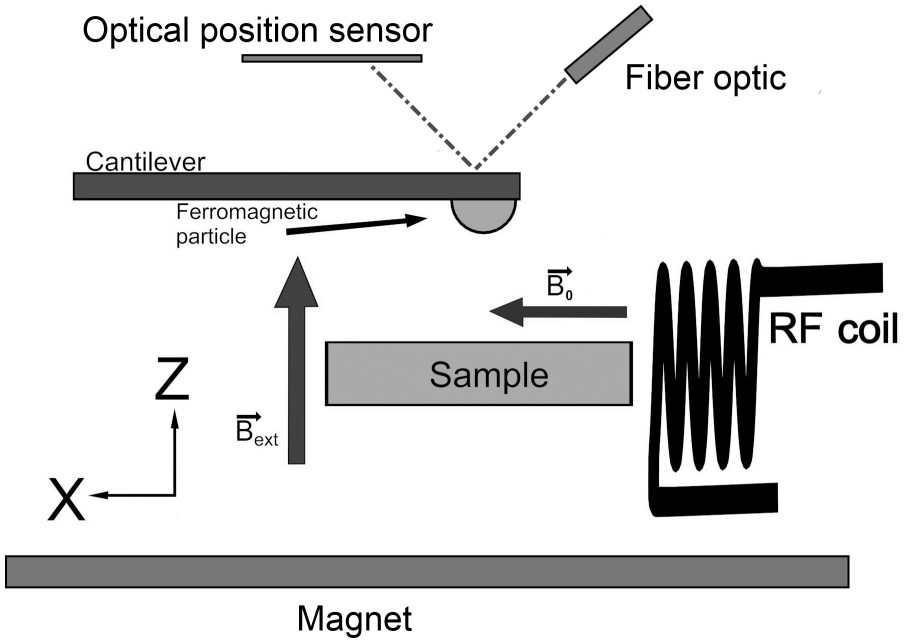

Figure 2.7: Example of MRFM apparatus.

2.2.5 Theory of Operation

In a typical MRFM experiment, the sample under test is located a short distance above or below the cantilever tip and the iron particle. As with an NMR experiment, the sample is within the close vicinity of a strong permanent magnet with a magnetic field strength of B_{ext} which induces Zeeman splitting within the sample. The ferromagnetic particle on the cantilever tip induces the required gradient in the otherwise homogeneous magnetic field as given by Eqn. 2.23, which in turn affects the dipole magnetic field, B_d, which acts between the FM particle and the individual spins within the sample. The spins within the sample which share the same dipole magnetic field strength form what is called the Resonance Slice which has a shape that is dictated by the shape of the FM particle. In this case, since the FM particle has a hemispherical shape, the resulting resonance slice will also have a hemispherical shape within the sample. The thickness of the resonance slice is directly proportional to the magnitude of the external magnetic field, B_{ext}. Since the spins within the resonance slice have the same B_d, Eqn. 2.26 shows that for a ω_{RF} of the appropriate frequency the spins within the resonance slice will absorb some of the RF energy and transition between the α and β states. Unlike NMR experiments where the RF pulse emitted from the sample during a β to α transition is detected using a receiving antenna, MRFM experiments measure the cantilever deflection due to the changes in the dipole magnetic force that acts between the spin in the sample and the ferromagnetic particle.

There are multiple considerations for the RF pulse techniques used to manipulate the magnetic moments of the sample under test, one such RF pulse consideration is a frequency modulated RF pulse. In MRFM experiments it is necessary to measure the motion of the cantilever tip, this leads to the ferromagnetic particle also being in motion. This results in the dipole magnetic force, B_d being in a state of constant fluctuation and indicates that for a fixed ω_{RF} the resonance slice will move within the sample in accordance with the FM particle movement during cantilever oscillations. In order to keep the resonance slice stationary while the cantilever beam is in motion, ω_{RF} needs to be modulated as it is pulsed through the sample during the cycle of the cantilever oscillation. Another consideration is that since the cantilever is always in motion, constantly applying the RF pulse will cause a near constant

force to act on the oscillating cantilever beam. However for detection purposes it is desirable to only apply a force on one of the up-swing or down-swing of the cantilever. This requires that the emitted RF pulse needs to be disabled during the cantilever up-swing and enabled on the cantilever down-swing or vice-versa. This harmonic force causes a resonance response on the cantilever resulting in a larger deflection. An example of the modulated RF pulse is shown in Figure 2.8 below.

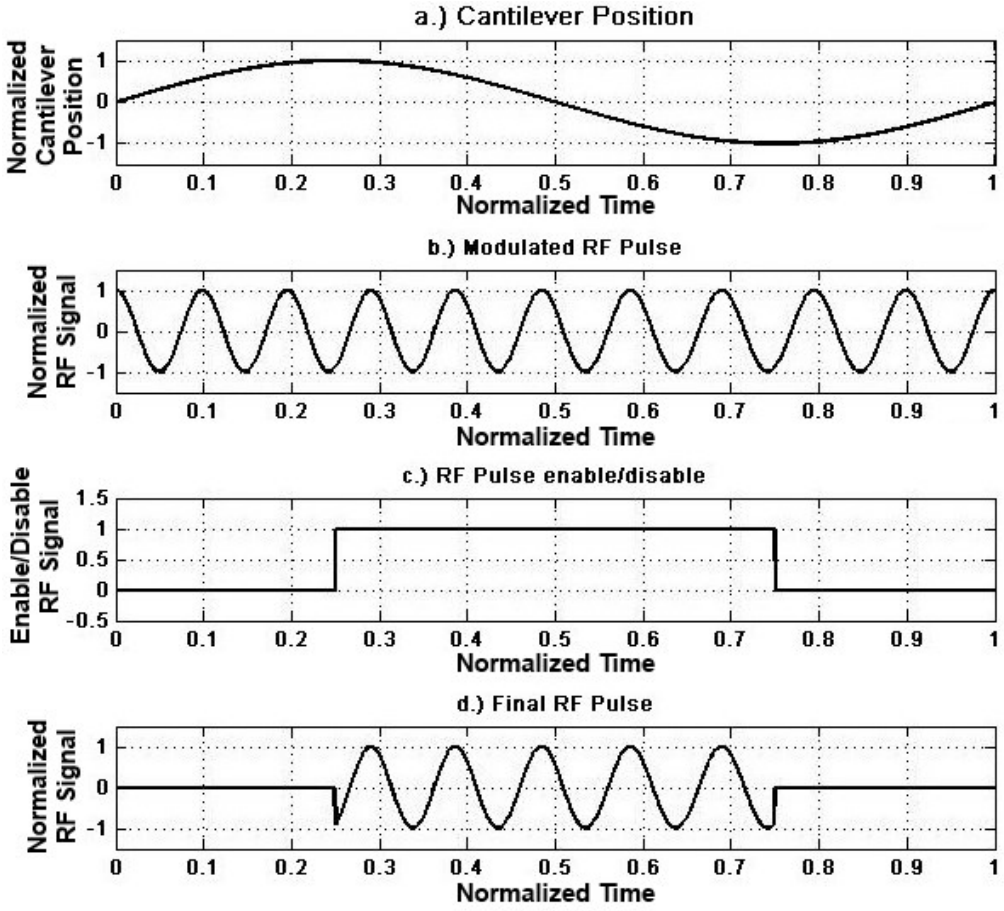

Figure 2.8: Pulsed RF pulse modulated to cantilever position: **a.** Cantilever Position **b.** RF waveform modulated to cantilever position **c.** RF pulse enabled during the downward motion of the cantilever beam **d.** Final RF waveform

Another consideration is the duration of the RF pulse. This sequence is based on the Rabi frequency of the spin under investigation, given by $\omega_R = \gamma B_0$ where B_0 is the magnetic field strength of the RF field. By applying an RF pulse with duration $t = \pi/\omega_R$ to the sample the magnetic moment(μ) of the spin reverses its orientation within the sample; in

MRFM experiments this is referred to as a π-pulse. If a sequence of π-pulses is applied to the sample, the direction of μ changes periodically with a period equal to twice the time interval between the π-pulses. If the magnetic moment is pointing in the direction of the FM particle, then the magnetic dipole force attracts the FM particle, whereas if the magnetic moment is pointing away from the FM particle, the dipole force repels the FM particle [4].

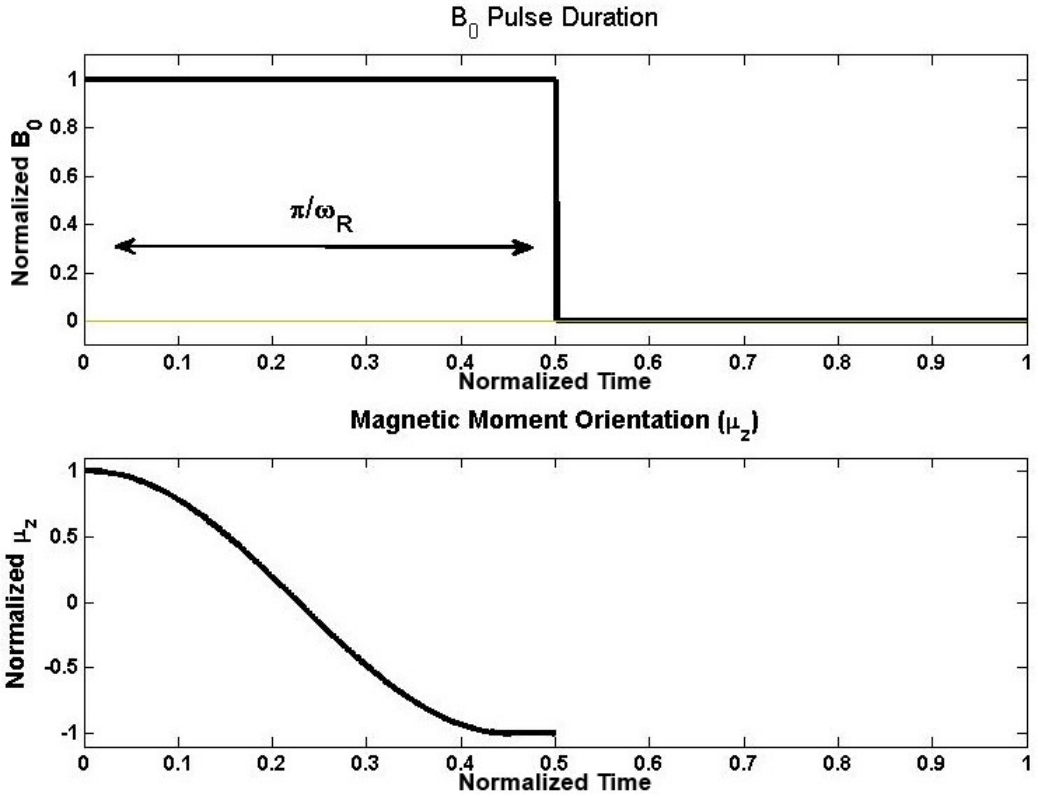

Figure 2.9: Amplitude of RF π pulse and the reaction of the magnetic moment.

It can be seen that by taking into consideration frequency modulation and using a periodic π-pulse, the applied RF pulse generates a periodic magnetic force that acts on the FM particle and the cantilever tip. If the period of this magnetic force is the same as the cantilever period, then the force will drive resonance vibrations of the cantilever. A measurable signal can be observed if the amplitude of the resonance vibration exceeds the amplitude of the thermal vibrations of the cantilever.

2.3 Botrytis Cinerea

Botrytis Cinerea is a fungal species which belongs to the Sclerotiniaceae family of fungus that affects over 200 plants including grape, strawberry, tomato and pepper crops [26]. The fungal infection on such crops is referred to as noble rot or grey mold disease, depending on when the initial stages of infection occur, and results in the surface of the host plant or fruit being covered in a fuzzy grey mold (Figure 1.1**a**). The spore composition of botrytis cinerea includes of a complex network of interior cell walls which isolates the spore membrane from toxins carried within. Once such toxin is botcinolide, which get secreted from the spore and is used to help break down the exterior layer of the host plant to ease the infection process [27]. Like other fungus, botrytis cinerea spores spread amongst hosts via air currents, ground water or insects carrying spores. The botrytis spore has a lemon shape with an average length of $12\mu m$ and an average diameter of $7\mu m$, as shown in Figure 1.1**b**, this results in an approximate volume of $226\mu m^3$ [28]. DNA based kits are available for detection of the botrytis cinerea fungus, however the spores can be glued to a surface using a specifically harvested antibody

2.3.1 Monoclonal Antibodies

Antibodies are a type of protein found in the immune system of animals to fight off infection due to viral, bacterial or fungal infection. The antibodies have a special receptor called a paratope which form chemical bonds between themselves and the epitope of the host infection [29]. There are various types of antibodies used in immunology, including polyclonal and monoclonal antibodies. Polyclonal antibodies are proteins that have paratopes which can interact and bond to multiple epitopes from different types of infections, making it ideal for collecting a broad range of potential infections. In contrast, the paratopes of monoclonal antibodies are cultivated to target a single type of epitope, which allows for a higher selectivity of the infection in which the antibody binds to [30]. Although the chemical interactions between paratopes and epitopes can be complex in nature, figure 2.10 gives a simplified visualization of paratope/epitope bonding.

BC-12.CA4 is a monoclonal antibody manufactured by the National Institute of Health in

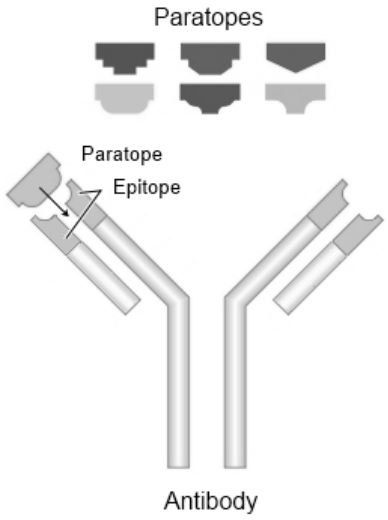

Figure 2.10: Visual depiction of monoclonal antibody binding. Note that while different paratopes exist only one can bind to the epitope

the USA and distributed by The Developmental Studies Hybridoma Bank at the University of Iowa. This antibody is harvested from the liver of mice and has paratopes which chemically binds specifically to the epitopes located on the exterior of the botrytis cinerea spore. A layer of the BC-12.CA4 antibody will be spread on the sensor such that the spores that enter the sensor and adhere to this layer are within the sensing range of the cantilever beam.

2.3.2 Solid State NMR of spore

In order to determine the organic hydrogen component of the botrytis cinerea spore, a solid state NMR was performed on a large number of the spores. The botrytis spores were grown and harvested by the spore lab at the University of Saskatchewan Department of Agriculture using 32 $8'' \times 5''$ aluminum trays and the following procedure. A piece of white bread was placed into each of the trays and autoclaved with high pressure steam for 20 minutes to sterilize the tray and bread. Once the trays cooled, 375 mL of autoclaved potato dextrose agar (PDA) was poured into each tray. The trays were then covered and left overnight to allow the PDA media to solidify. The botrytis serum was prepared using isolated botrytis cinerea spores and has a concentration of approximately 2.0×10^5 spores per mL; 5 mL of the serum was spread on each tray. A piece of autoclaved aluminum mesh

was then placed directly on the media to allow the vegetative parts of the fungus to grow through. The trays were incubated at 21 $^{\circ}C$ in the dark for two weeks.

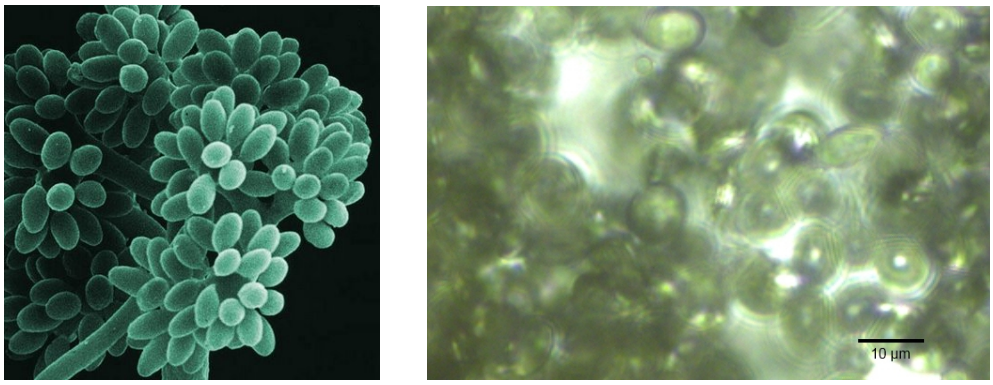

(a) (b)

Figure 2.11: Botrytis cinerea spores **a.** attached to the conidia. **b.** harvested by vacuum process

After the two week incubation period the spores were separated from the conidia and collected using a vacuum system with a small collection cylinder equipped with a Whatman grade 1 ($11\mu m$) filter paper. Figure 2.11 shows the botrytis spores attached to the conidia and the spores after collection with the vacuum. The collected spores were then dried in an oven at $32^{\circ}C$ for several hours to remove excess moisture. The spores were then transferred to the magic-angle spinning (MAS) rotor used for the solid state NMR using the packing tools which came with the rotor. Two batches of spores were examined using the 360 MHz Bruker Avance spectrometer with solid state NMR capabilities shown in Figure 2.12**a** owned and operated by the NMR lab at the National Research Council located at the University of Saskatchewan. The experiment was performed using the 4mm Cross Polarization MAS probe shown in Figure 2.12**c**. Figure 2.12**b** shows the MAS rotor used (on left, beside the ruler), funnel and packing tool (top center and right) and the cap removal tool (bottom center) used. The rotor is made from zincronium and has a Kel-F cap, both materials are used because of their lack of hydrogen atoms and are a standard for solid state NMR.

The spectra acquired using the solid state NMR are given in Figures 2.14 and 2.15 for the first and second batches of spores run. Both spectra indicate that there is a large concentration of organic hydrogen within the botrytis spore, suggesting that there are numerous ^{1}H

(a)

(b)

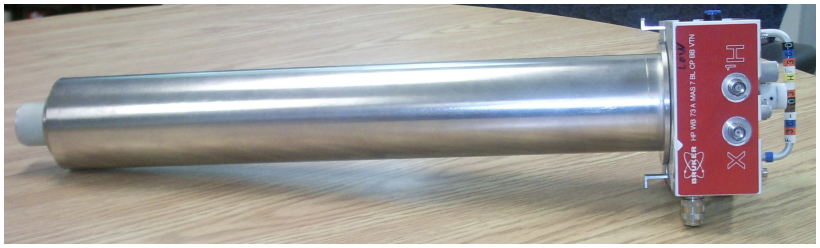

(c)

Figure 2.12: Tools used in MNR experiment: **a.** 360 MHz Bruker Avance spectrometer, **b.** MAS rotor and packing tools, **c.** 4mm Cross Polarization MAS probe.

spins which can be manipulated by the proposed MRFM based sensor. Using Shoolery's rule on the chemical formula for botcinolide (Figure 2.13) it is possible to estimate the chemical shift for the CH_3 molecules. The chemical shift of the CH_3 molecules labelled 'a' through 'e' on Figure 2.13 are estimated using Shoolery's rule and the spectral peaks in Figures 2.14 and 2.15 are labeled accordingly. It is easy to see that all the points except point 'e' belong to the broad peak range between 3.0 and 7.5 ppm. The broad peak is a result of the electrons which travel along the carbon ring portion of the botcinolide molecule. The electron motion about the ring acts as a large current loop within the structure, which magnetically shields the hydrogen atoms attached to the ring. The different orientations between the external magnetic field and the carbon ring results in a broadening of the spectral peak.

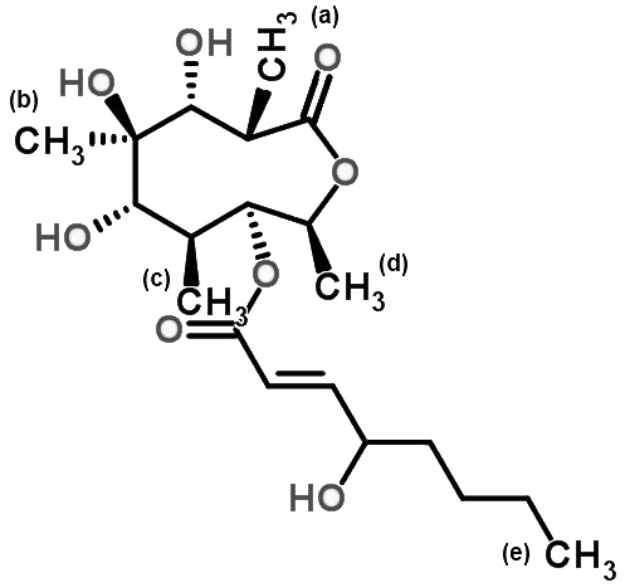

Figure 2.13: Chemical formula for botcinolide

Table 2.4: Chemical shifts for CH_3 molecules of botcinolide.

CH_3 (a)	$CH_2 - H - O - OH$	$0.23 + 0.17 + 2.36 + 2.56$	5.32	ppm
CH_3 (b)	$CH_2 - H - OH - OH$	$0.23 + 0.17 + 2.56 + 2.56$	5.52	ppm
CH_3 (c)	$CH_2 - H - CO - OH$	$0.23 + 0.17 + 1.70 + 2.36$	4.66	ppm
CH_3 (d)	$CH_2 - H - CO - CO$	$0.23 + 0.17 + 1.70 + 1.70$	3.80	ppm
CH_3 (e)	$CH_2 - H - C = C$	$0.23 + 0.17 + 1.32$	1.72	ppm

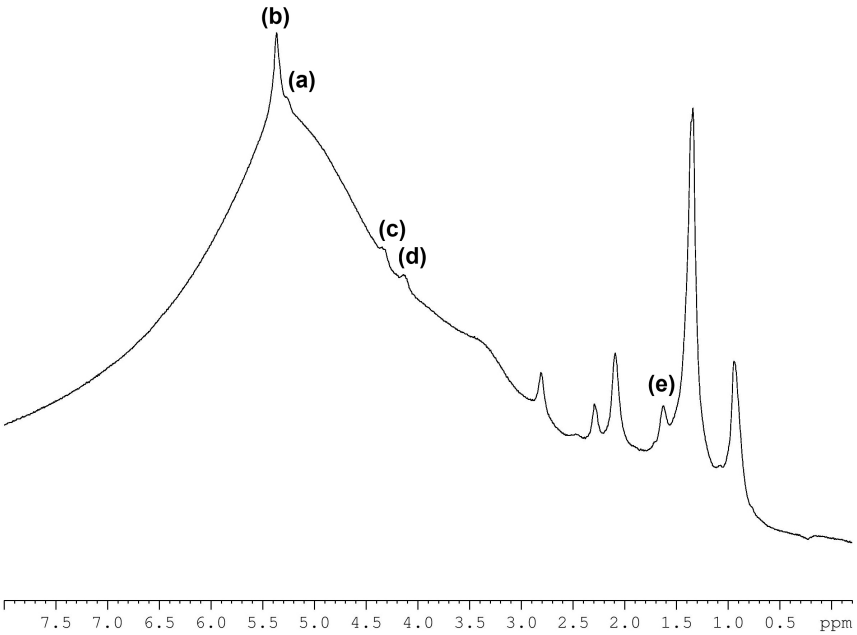

Figure 2.14: Solid NMR spectrum of the first batch of botrytis cinerea spores. The peaks labelled 'a' through 'e' correspond to the respective CH_3 molecule in Figure 2.13 and calculated using Table 2.4.

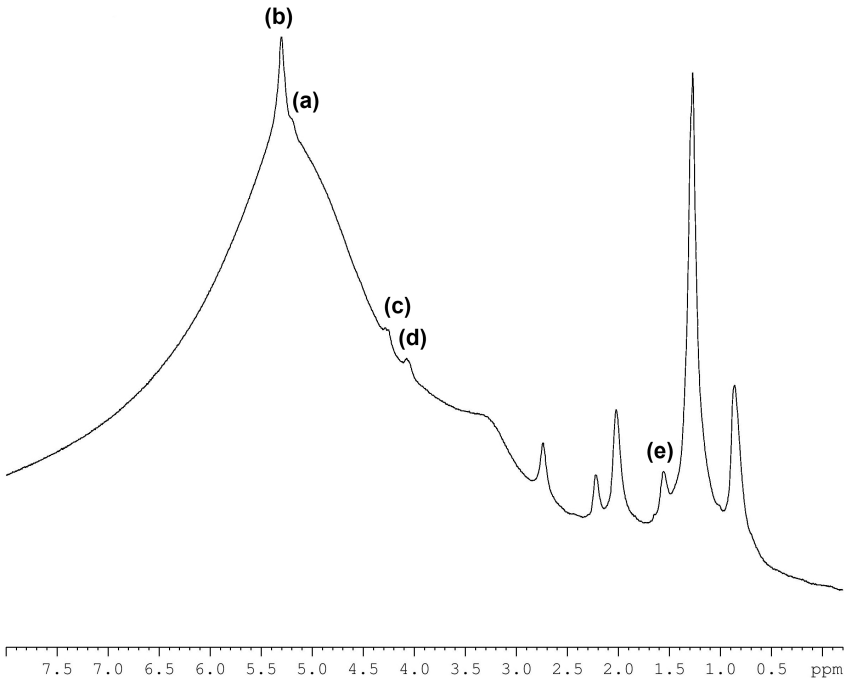

Figure 2.15: Solid NMR spectrum of the second batch of botrytis cinerea spores. The peaks labelled 'a' through 'e' correspond to the respective CH_3 molecule in Figure 2.13 and calculated using Table 2.4.

3. Simulation and Results

In order to determine the feasibility of the proposed mold spore sensor, multiple simulations were performed to determine the response of the sensor and revise the design characteristics. The sensitivity of the sensor is heavily reliant on the characteristics of the cantilever beam such as spring constant, resonant frequency and mechanical quality factor. A minimal change in one parameter of the cantilever beam can affect several others, sometimes with drastic effects. In order to track the effects of parameter changes and maximize the sensitivity, simulations were performed to estimate the operating characteristics for the proposed sensor and estimate the dipole magnetic force which occur from a magnetic resonance force microscopy experiment.

Two simulation tools were used to determine the characteristics of the sensor. MATLAB® was used to determine the force which acts between the sample and the ferromagnetic particle attached to the paddle of the cantilever. MATLAB was also used to estimate the cantilever dimensions, the resulting natural resonance frequency and various damping mechanisms. COMSOL Multiphysics® was used to verify the operation of the cantilever beam as well as verify the damping factors which affect the cantilever. A time domain analysis was performed on the cantilever structure in COMSOL and was used to calculate the response of the cantilever beam when under the influence of the load estimated by the MATLAB script.

The simulations and calculations done compared two cantilever beams made from two different materials, silicon and silicon nitride. Table 3.1 outlines the key properties of these materials. At the end of the cantilever beam is a square paddle with dimensions of $10\mu m \times 10\mu m$ and a thickness equal to the thickness of the cantilever beam. At the center of the paddle is a hemispherical ferromagnetic particle made of iron with a radius of $1.5\mu m$. It

is assumed that the sensor will be required to operate in an outdoor environment at a temperature up to $300°K$ $(26.85°C)$. The properties for the iron particle and operating environment of the cantilever beam are given in Table 3.2. The first step in the design of the proposed sensor is to determine the cantilever dimensions and the magnitude of the magnetic force which results from a MRFM experiment, both of which were estimated using MATLAB.

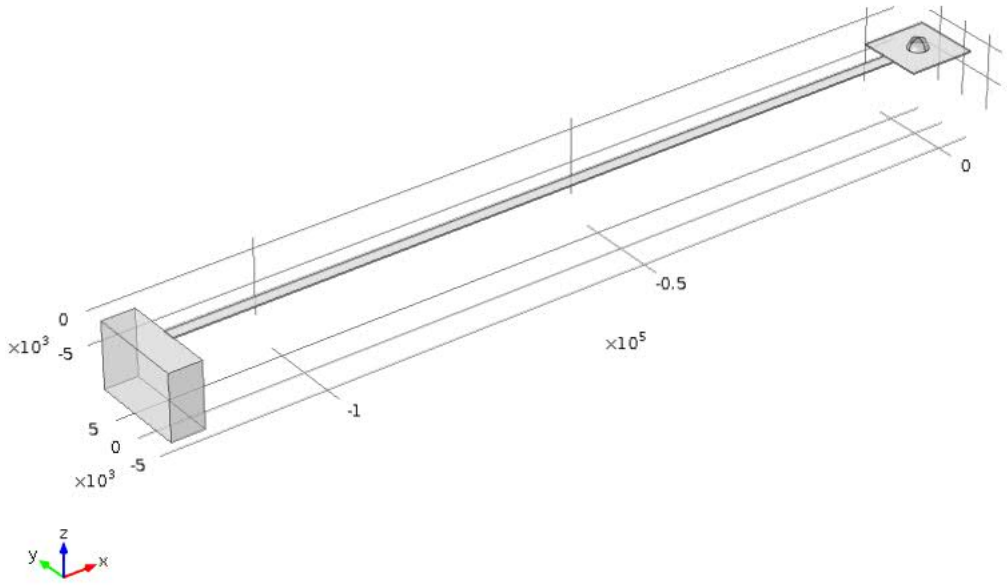

Figure 3.1: MEMS cantilever used for magnetic resonance force microscopy

3.1 MATLAB

MATLAB was used to estimate the properties of the MEMS cantilever. The MATLAB script inputs a target for natural resonance frequency, then uses the material properties given in Table 3.1 and 3.2 and a combination of Eqn. 2.5a through 2.22 the script estimates the dimensions, mass and critical damping of the MEMS cantilever. As the dimensions of the cantilever beam changes, so does the mass and spring constant of the beam and therefore the resonance frequency of the beam. The script starts by estimating the spring constant

Table 3.1: Material properties of silicon and silicon nitride [18].

	Quantity	Symbol	Value
Silicon	Density ($\frac{kg}{m^3}$)	ρ	2330
(Si)	Young's Modulus (GPa)	E	170
	Coefficient of thermal expansion($\frac{1}{^\circ K}$)	α	2.6×10^{-6}
	Thermal conductivity ($\frac{W}{m\,^\circ K}$)	κ_{th}	130
	Specific heat capacity ($\frac{K}{kg^\circ K}$)	C_p	700
Silicon Nitride	Density ($\frac{kg}{m^3}$)	ρ	3100
(Si_3N_4)	Young's Modulus (GPa)	E	250
	Coefficient of thermal expansion($\frac{1}{^\circ K}$)	α	2.3×10^{-6}
	Thermal conductivity ($\frac{W}{m\,^\circ K}$)	κ_{th}	20
	Specific heat capacity ($\frac{K}{kg^\circ K}$)	C_p	700

and resonance frequency of the cantilever beam alone, then the mass of the paddle and iron particle attached to the end of the cantilever beam and the resonance frequency is recalculated. The script then modifies the dimensions of the cantilever beam in order to get the resonance frequency of the cantilever beam to approach the desired target frequency. Figure 3.2 shows the flowchart of the script used to estimate the cantilever properties. For these calculations, the cantilever thickness was fixed at 200 nm, which helps considerably to reduce the spring constant of the cantilever while maintaining the structural integrity of the beam.

Table 3.2: Material properties of iron and the operating environment of cantilever beam.

	Quantity	Symbol	Value
Iron	Density ($\frac{kg}{m^3}$)	ρ	7860
(Fe)	Radius (μm)	r	1.5
Operating Environment	Temperature ($^\circ K$)	T_0	300
(Air)	Pressure (Pa)	P_0	300

The script also takes into account the operating temperature and pressure of the cantilever environment which are used to calculate the dynamic viscosity, density and mean free path of the fluid surrounding the cantilever beam, in this case air. The script then estimates the individual mechanical quality factors for clamping, thermoelastic, Stoke's and squeeze film damping using a combination of Eqn. 2.13 through 2.19. In the interest of minimizing the effects of air damping the operating pressure of the cantilever beam is assumed to be 300 Pa. This operating pressure is maintainable using a rotary-valve vacuum pump and can be sealed within the sensor packaging if capped using the techniques introduced in Section 4.5. From the quality factors calculated the script estimates the total quality factor of the cantilever setup. The script then modifies the cantilever dimensions in order to maximize the total quality factor of the cantilever setup. The cantilever dimensions obtained through this script will be inputted into COMSOL for verification and as a starting point for additional simulations performed using that software, which is discussed in the next section.

A second MATLAB script uses a number of equations from Sections 2.1 and 2.2 to estimate location of the resonance slice within a sample and determine the dipole magnetic force that acts between the resonance slice and the iron particle. The samples used for the simulation were blanks with a homogeneous distribution of hydrogen atoms. The distance between hydrogen atoms within the sample is assumed to be 2.2 nm, which is approximately twenty times the length of the average hydrogen-carbon bond and gives an approximate spin density of 9.6 $\frac{spins}{100nm^3}$ [31]. The spin density is then inserted into the Boltzmann distribution given in Eqn. 2.5a resulting in a reduced spin density of 2.4 $\frac{spins}{nm^3}$ at an operating temperature of $300°K$ and a magnetic field strength of 0.9 Tesla. Next the script calculates the distance between the spins within the sample and the iron particle assuming there is only air between the two.

Using the position of the spins, the script calculates the RF frequency required to invoke the resonance reaction at the top and bottom faces of the sample. The script then cycles through multiple iterations of the applied radio frequency equally spaced between the maximum and minimum frequencies determined in the previous step. During each iteration the dipole magnetic field is calculated at each individual spin, which is then checked using Eqn.

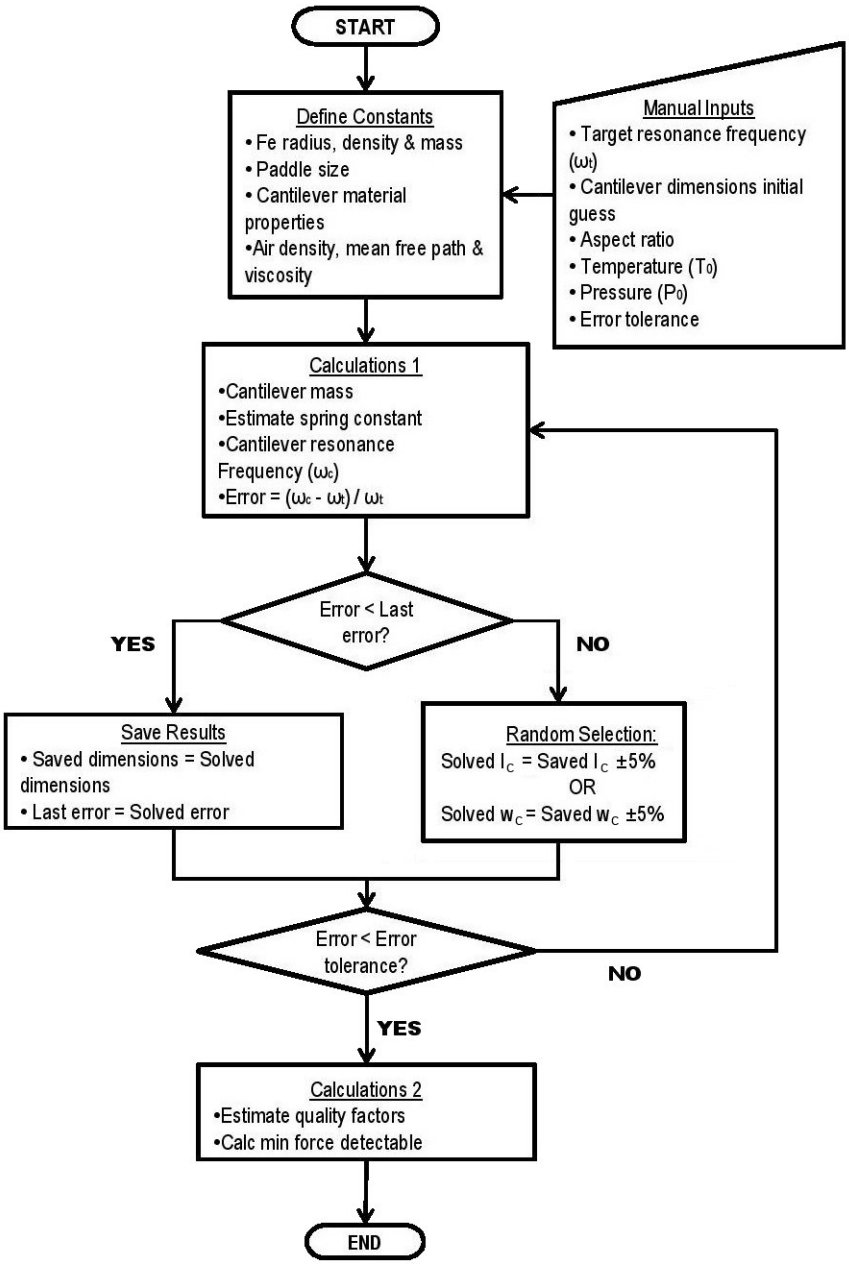

Figure 3.2: Flowchart for determining cantilever dimensions from material properties and target resonance frequency

2.26 to see if the resonance condition is satisfied. If the resonance condition exists the script calculates the magnetic field gradient at that spin location and estimates the z-component of the dipole magnetic force which acts between the spin and the iron particle. The script finishes by summing the individual forces from each spin resulting in the net dipole magnetic field which acts between the spins in the resonance slice and the ferromagnetic iron tip at

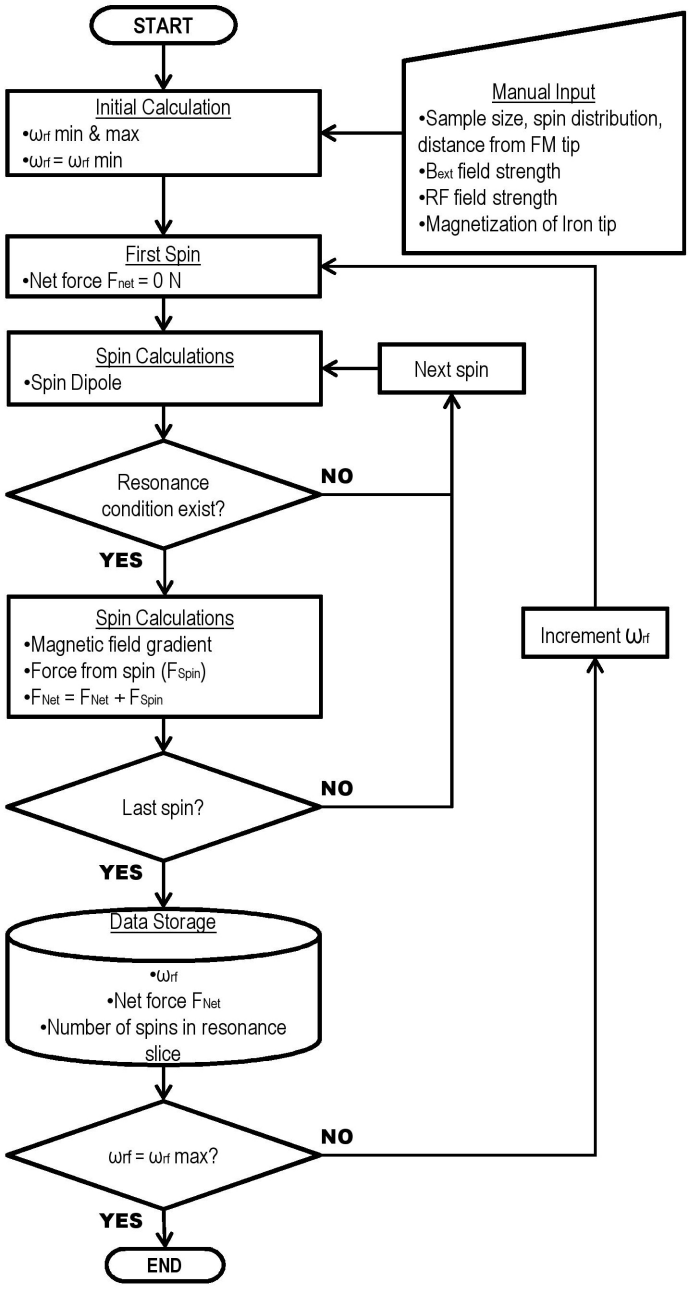

Figure 3.3: Flowchart for determining dipole magnetic force between sample and iron tip.

the tested RF frequency. Figure 3.3 shows the flowchart for this second MATLAB script.

3.2 COMSOL Multiphysics

COMSOL Multiphysics (previously known as FEMLAB) is a simulation tool that utilizes finite element analysis and coupled partial differential equations to simulate an assortment of physics applications for a number of topics including electric, magnetic and structural and fluid dynamics. For this study COMSOL was used to verify the cantilever design using eigen frequency, frequency domain and time domain analysis. Using the structural mechanics module, an eigen frequency analysis calculates the resonance frequencies and the shapes of the structure at those modes. This design requires the fundamental mode of cantilever oscillation, which corresponds to λ_1 given in Section 2.2.1.

Once the cantilever dimensions and resonance frequency were verified, the thermal stress module was used to estimate the thermoelastic damping of the cantilever caused by localized stress/strain as the beam oscillates. A thin-film boundary condition was added to the model to simulate the air gap that the cantilever operates in. By specifying the operating environment of the cantilever beam and the surrounding medium COMSOL is able to include the effects of both Stoke's and squeeze damping which acts on the beam as well. The cantilever quality factor can be estimated from the COMSOL simulations by using the results of the frequency analysis spectrum and Eqn. 3.1 where f_0 is the frequency where the maximum displacement occurs and Δf is the difference between the frequencies where the displacement is half of the maximum deflection.

$$Q = \frac{f_0}{\Delta f} \tag{3.1}$$

Once the cantilever behavior has been determined, the force/frequency spectrum acquired from the second MATLAB script was inserted into the COMSOL model to interpolate the applied magnetic force upon the ferromagnetic particle for a given operating frequency. Using these conditions a time-domain analysis of the model was run to determine the time necessary for the cantilever to move from its rest position to sustainable harmonic oscillations with an amplitude greater than twice the theoretical amplitude of thermal vibration of the beam.

3.3 Results and Discussion

In the first MATLAB script, the target resonant frequency of the cantilever beam was 10 kHz. The beam was fixed at one end and had an attached load at the other end. The load mentioned is the $10\mu m \times 10\mu m$ paddle and the attached iron particle. Once the script determined the dimensions of the cantilever which gives the desired resonance frequency, the script then take temperature and pressure inputs and calculates the properties of the surrounding air. This information was used to estimate the quality factor of the cantilever within the defined environment. This script was run for both silicon and silicon nitrite; the operating parameters and results are shown in Table 3.3

Table 3.3: Calculated parameters from MATLAB script

Environmental Parameters and Constants			
Temperature		300	$(^\circ K)$
Pressure		300	(Pa)
Target Cantilever Freq.		10	(kHz)
Cantilever Thickness		200	(nm)
Cantilever Pad Size		10 x 10	(nm)
External Magnetic Field		0.9	(T)
Results	**Si**	$\boldsymbol{Si_3N_4}$	
Cantilever freq.	9.982	10.006	(kHz)
Cantilever length	116.7	119.5	(μm)
Cantilever width	2.12	2.17	(μm)
Spring Constant	454×10^{-6}	636×10^{-6}	$(\frac{N}{m})$
$Q_{Squeeze}$	1311.3	1674.6	
Q_{Stokes}	36.2	48.3	
$Q_{Themoelastic}$	35.1	105.7	
Q_{Clamp}	417.2×10^{9}	447.9×10^{9}	
Q_{Total}	31.6	32.51	
Min detectable force	544.5×10^{-3}	804.9×10^{-3}	(fN)

Once the cantilever dimensions are estimated, they were imported into COMSOL for additional refinement. An eigen frequency analysis on the parameters given in Tables 3.1 and 3.3 results in a slight variation of the cantilever resonance frequency. The main reason for this deviation is due to the mass distribution between the fixed and free end of the cantilever. Once the cantilever dimensions have been updated, a stationary analysis was done on the cantilever to determine the natural deflection of the cantilever under the weight of the iron particle alone. In order to determine the spring constant for the cantilever beam, an incremental force was applied to the iron particle and the stationary deflection was calculated again, then using the relationship $\delta = \frac{F}{k}$ [18] where δ is the deflection of the cantilever tip and F is the force applied to the end of the cantilever beam. The result of the above analysis for both silicon and silicon nitride is given in Table 3.4.

Table 3.4: Calculated parameters from COMSOL model

	Si	$\boldsymbol{Si_3N_4}$	
Cantilever length	107.1	114.8	(μm)
Cantilever width	2.00	2.00	(μm)
Cantilever freq.	10.010	10.006	(kHz)
Spring Constant	79.1×10^{-6}	80.6×10^{-6}	$(\frac{N}{m})$
Natural deflection	2.77	2.82	(nm)

The next step of the analysis is to apply a small (-50 fN) harmonic load upon the iron particle to determine the quality factor of the cantilever at and around the resonant frequency. The frequency domain analysis calculates the deflection of the cantilever tip as the harmonic load is applied over a range of frequencies. The results of the analysis in Figure 3.4 shows that with a 50 fN harmonic force, the silicon cantilever will have a maximum deflection of 277 nm and the silicon nitride cantilever has a maximum deflection of 290 nm. These results indicate quality factors of 57.8 and 59.9 for the Si and Si_3N_4 cantilevers respectively given only stress-strain and clamp damping only.

In order to incorporate Stokes and squeeze film damping into the model, a squeeze-film boundary layer was added to the cantilever beam. This boundary condition takes into

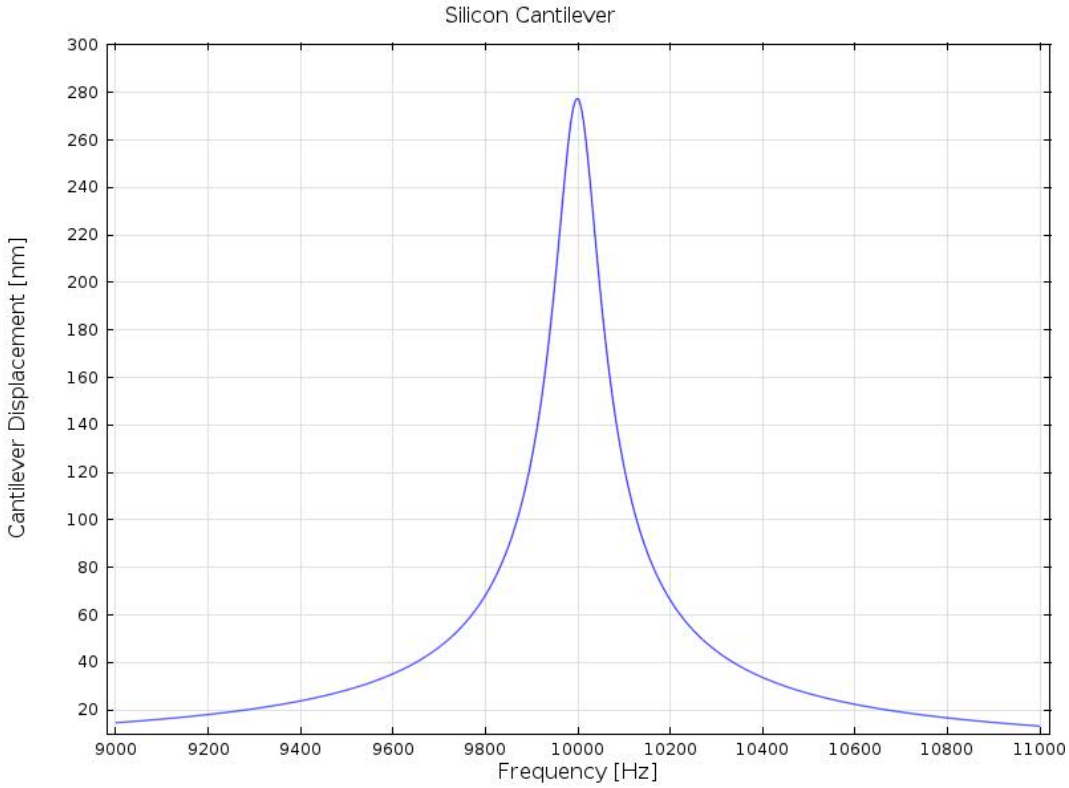

(a)

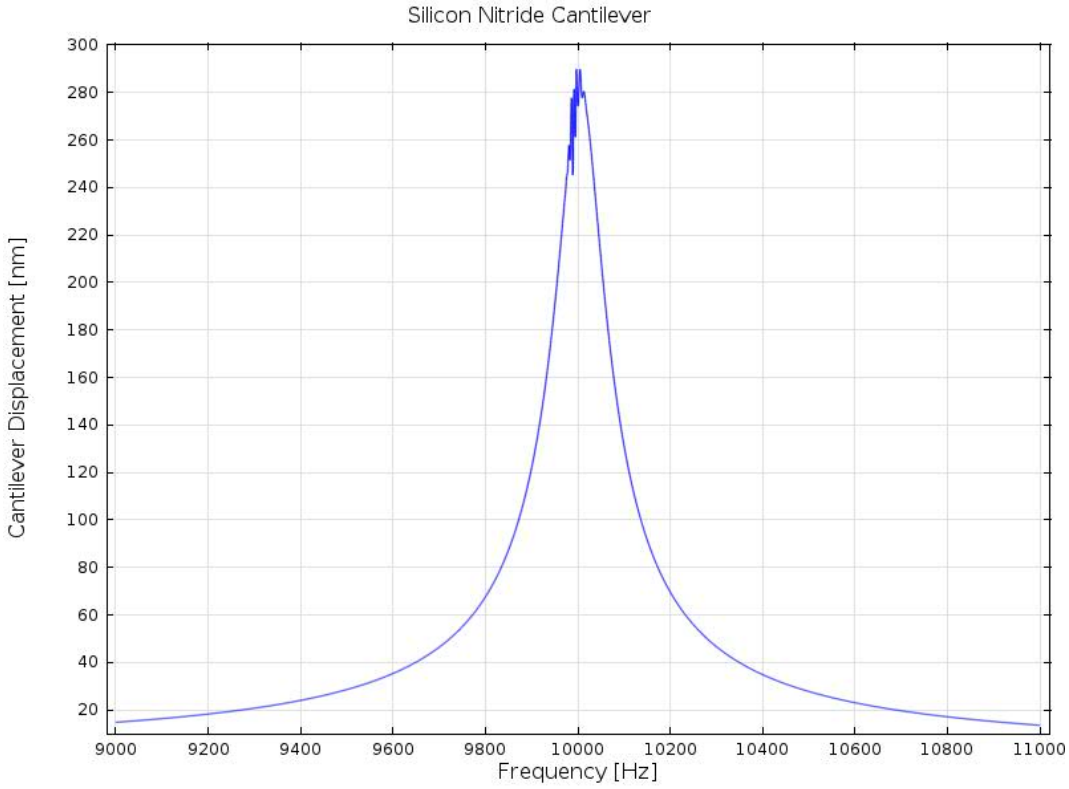

(b)

Figure 3.4: Results of the minimally damped frequency analysis of **a.** Silicon cantilever **b.** Silicon nitride cantilever

account the density and temperature of the surrounding air as well as the size of the air gap to apply damping and drag forces upon the cantilever beam as it oscillates. The thermal stress module was imported into the model and used to add the effects of thermoelastic damping to the cantilever beam. Another frequency analysis was performed on the model to calculate the quality factor of the fully damped system. The results of the fully damped simulation are presented in Figure 3.5 and shows that the silicon cantilever will have a maximum deflection of 140 nm and a mechanical quality factor of 28.7. In comparison the simulations show that the silicon nitride cantilever has a maximum deflection of 140 nm and a quality factor of 30.0.

Once the cantilever parameters were finalized, the second MATLAB script was used to calculate the dipole magnetic force which acts between the iron particle and spins in the sample where the resonance condition exists. The script defined the external magnetic field, B_{ext}, as 0.9T and the emitted RF field, B_0, at 300 μT. The script used was first tested using a cube shaped blank of size $2\mu m \times 2\mu m \times 2\mu m$ with a spin density of $9.4\frac{\text{spins}}{100nm^3}$ and a distance from the iron particle of $2\mu m$. The script calculated that for the given conditions, the ^{1}H spins produce an estimated maximum force of 380 fN when the RF pulse is 38.44 MHz, shown in Figure 3.6**a**. Notice the resonance slice given in Figure 3.6**b** is symmetrical about both the x and y axis assuming the center of the sample is located directly beneath the iron particle. This symmetry will be used in the next run of this script where the sample size is much larger. During this script run, it was found that the gradient of the magnetic field ranged from 10,000 $\frac{T}{m}$ at the bottom face of the blank to 100,000 $\frac{T}{m}$ at the top surface.

The second run of this script was performed on a lemon shaped botrytis spore. The volume of the botrytis blank is approximately 40 times larger than the volume of the square blank used in the last simulation run. In the interest of reducing the run time of the simulation which increases drastically with the volume of the sample, the simulations take advantage of the symmetry of the resonance slice noted above and run the simulation on a 1/4 section of the botrytis blank cut about the X and Y axis.

The script assumed that the top of the sample was located 5 μm above the cantilever in its stationary position and the results are presented in Figure 3.7**b**. At this position the

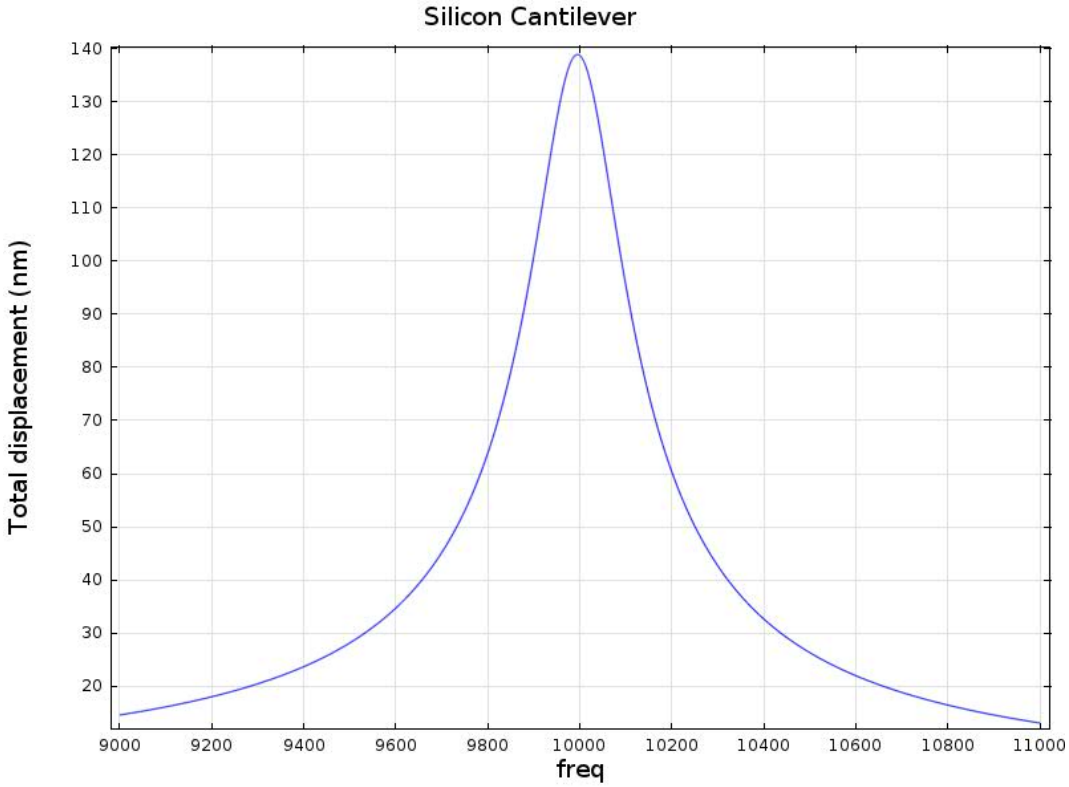

(a)

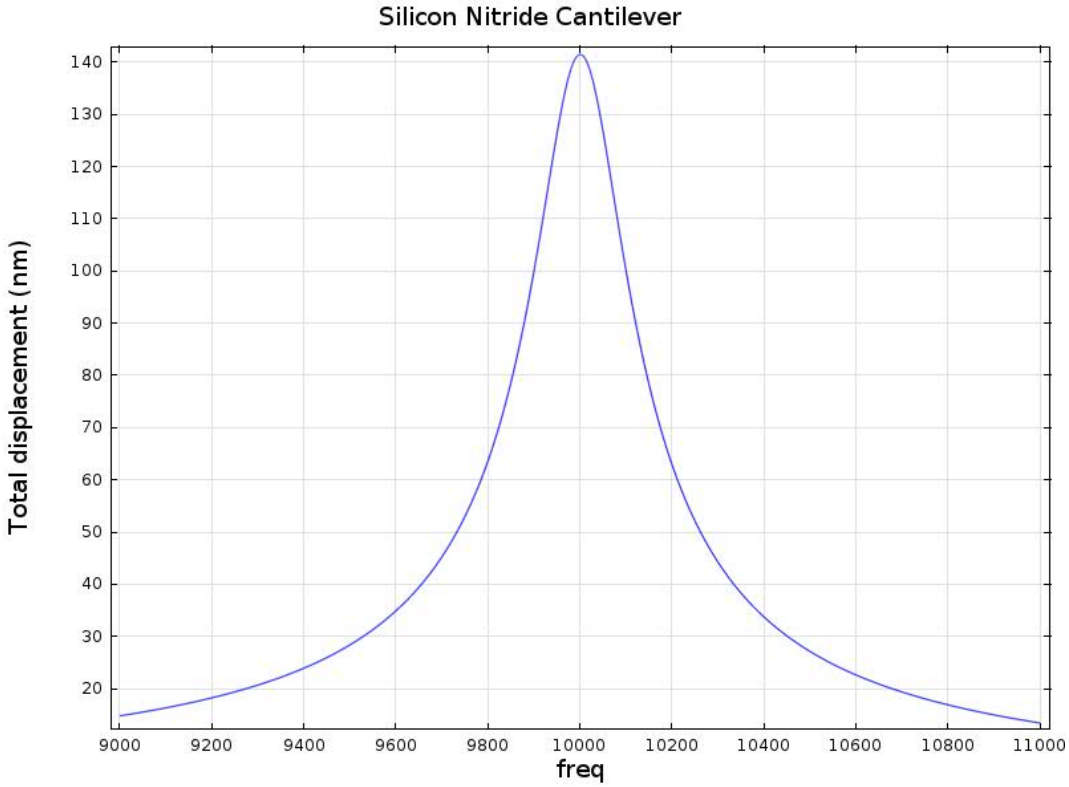

(b)

Figure 3.5: Results of the fully damped frequency analysis of **a.** silicon cantilever **b.** silicon nitride cantilever

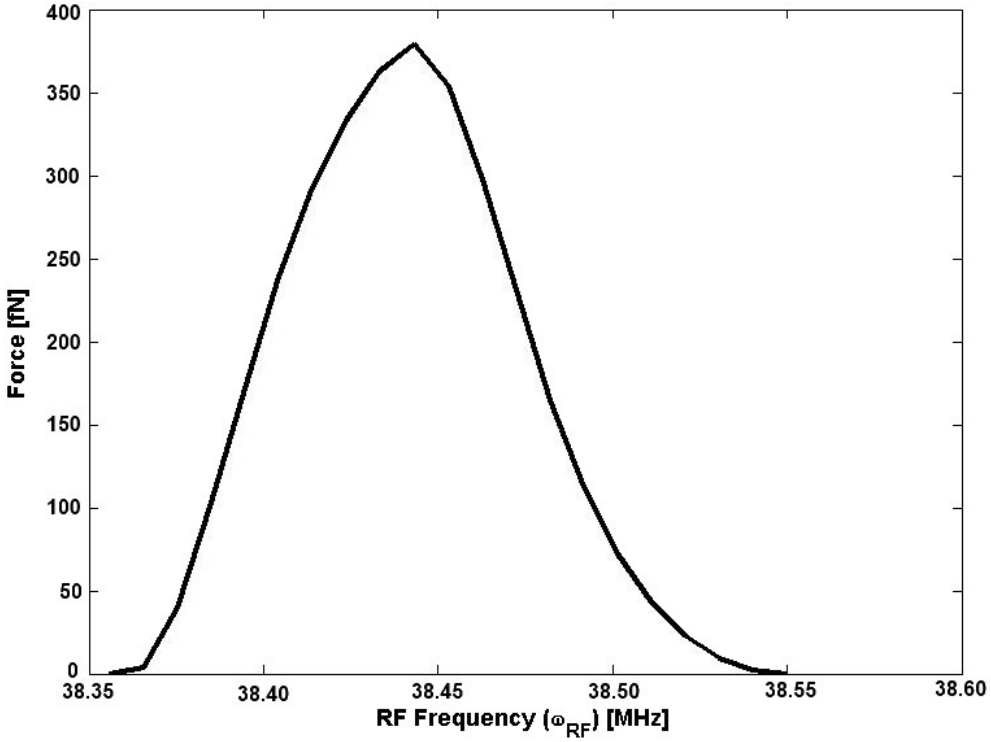

(a)

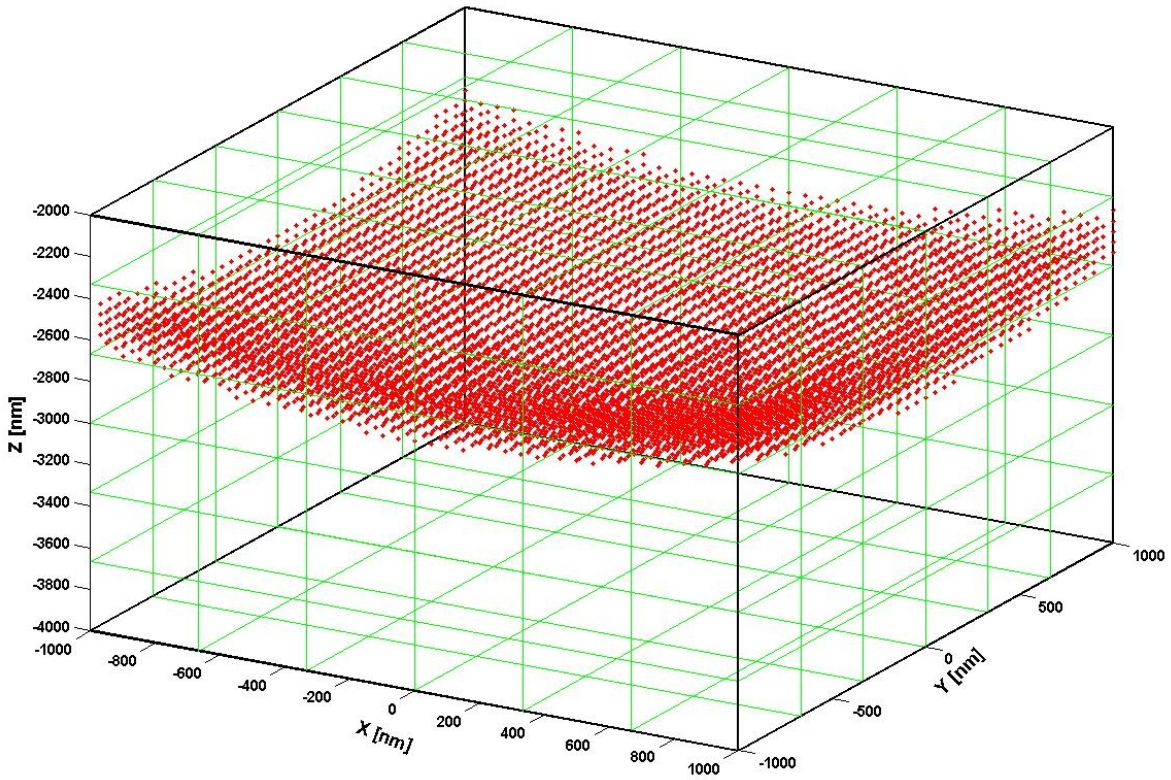

(b)

Figure 3.6: Magnetic resonance force microscopy results for a $2\mu m \times 2\mu m \times 2\mu m$ homogeneous blank **a.** Dipole magnetic force spectrum estimated for a given frequency **b.** location of the resonance slice at 38.44 MHz

force which acts upon the cantilever has a maximum of approximately 340 fN at 38.372 MHz and a measurable force is generated between 38.29 MHz and 38.60 MHz. The script was then re-run with the cantilever displaced by $\pm 1\mu m$ to determine the change in the resonance frequency as the cantilever oscillates. Referring to Figure 3.7**b** it can be shown that when the cantilever is oscillating, the frequency modulation of the RF pulse needs to swing between 38.35 MHz and 38.39 MHz at a rate of 16 Hz/nm of cantilever swing and the resulting dipole force can oscillate between 480 fN and 230 fN at a rate of approximately 0.1257 fN/nm.

When comparing the results from the $2\mu m \times 2\mu m \times 2\mu m$ cubed blank with a $2\mu m$ separation and the spore shaped blank $5\mu m$ from the cantilever tip, there are a number of similarities and differences in the resulting force spectra. The first similarity to notice is that frequency which results in the maximum force have comparable values (65 kHz difference), this is because Eqn. 2.26 is dominated by B_{ext} and reinforces the concept the external magnetic field determines the operating frequency of the RF pulse. Another similar feature between the two simulations is the maximum dipole magnetic force which occurs are comparable (35 fN difference) while the separation between the cantilever tip is significantly different. This feature is due to the result of the physical size of the sample. For the botrytis blank, the number of spins in the resonance slice is approximately an order of magnitude larger than the number of spins in the cube blank, so while the dipole magnetic force of each individual spin is small, the resulting magnetic force from all the spins in the resonance slice is much larger.

The differences between the two spectra give information about the shape of the sample. The slope of the force spectrum in Figure 3.7**a.** is steeper than the slope in Figure 3.6**a.**. This is due to the shape of the resonance slice as is passes through the sample at each step in the RF frequency. The resonance slice, which has a hemispherical shape, enters the bottom face of the cube blank in a ring shape fashion. As the RF frequency increases the resonance slice shifts upwards and more of the slice enters the sample, and eventually the slice exits the sample cube out the upper face. When the resonance slice enters and exits the sample, the number of spins which make up the resonance slice increases or decreases at a small rate, which gives a shallow slope on the force-frequency spectrum. In comparison, the number

of spins in the resonance slice that enters or exits the lemon shaped botrytis spore blank increases and decreases more rapidly due to the concave shape of the slice and the bottom surface of spore, which results in steeper slopes on the force-frequency spectrum.

Using the information obtained in the previous simulations, the final simulation of the sensor involves inputting the data from the MATLAB MRFM simulation of the botrytis spore into a time dependent study was performed on the cantilever structure in COMSOL. The interpolated force is applied to the iron particle which induces harmonic oscillations in the cantilever beam. As the cantilever oscillates, the applied RF pulse is modulated on and off such that the dipole magnetic force is applied while the cantilever is in its down-swing to increase the amplitude of the oscillation. Using Eqn. 2.21 and the cantilever values in Table 3.4 it is estimated that the amplitude of the thermal vibrations is approximately 5 nm. Figure 3.8 shows that when a harmonic load of 100 fN (RF frequency of approximately 38.3 MHz) is applied to the silicon nitride cantilever, the harmonic oscillations overcome the thermal noise and reaches 10 nm after the RF pulse has been applied for approximately 4 ms, this displacement increases to 60 nm after 22 ms. The silicon cantilever has a thermal oscillation amplitude of approximately 4 nm and the same harmonic oscillations reach an amplitude of 8 nm in 5 ms and an amplitude of 60 nm in 18 ms, the harmonic response of the cantilever is shown in Figure 3.9.

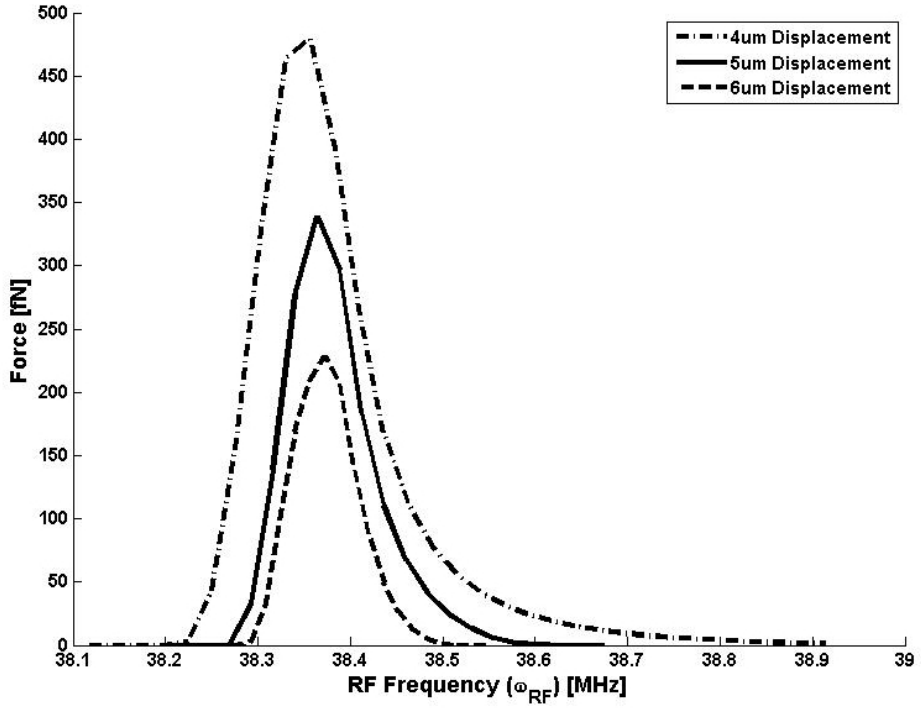

(a)

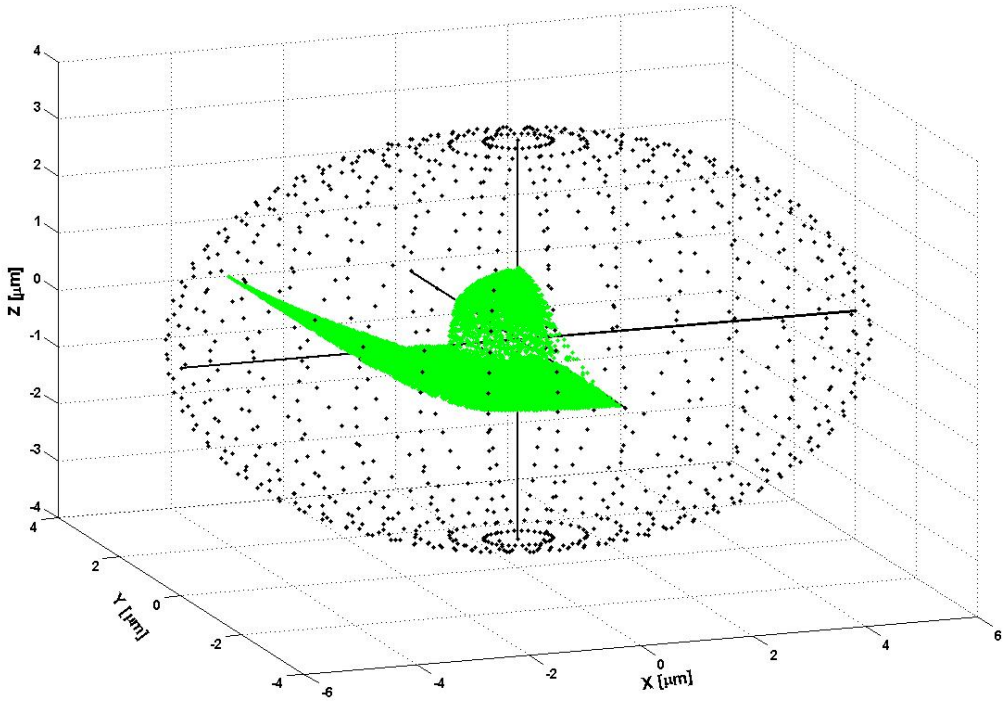

(b)

Figure 3.7: Magnetic resonance force microscopy results for the botrytis spore blank **a.** Force spectrum of sample located $4\mu m$, $5\mu m$ and $6\mu m$ from the cantilever. **b.** Location of resonance slice at 38.375 MHz.

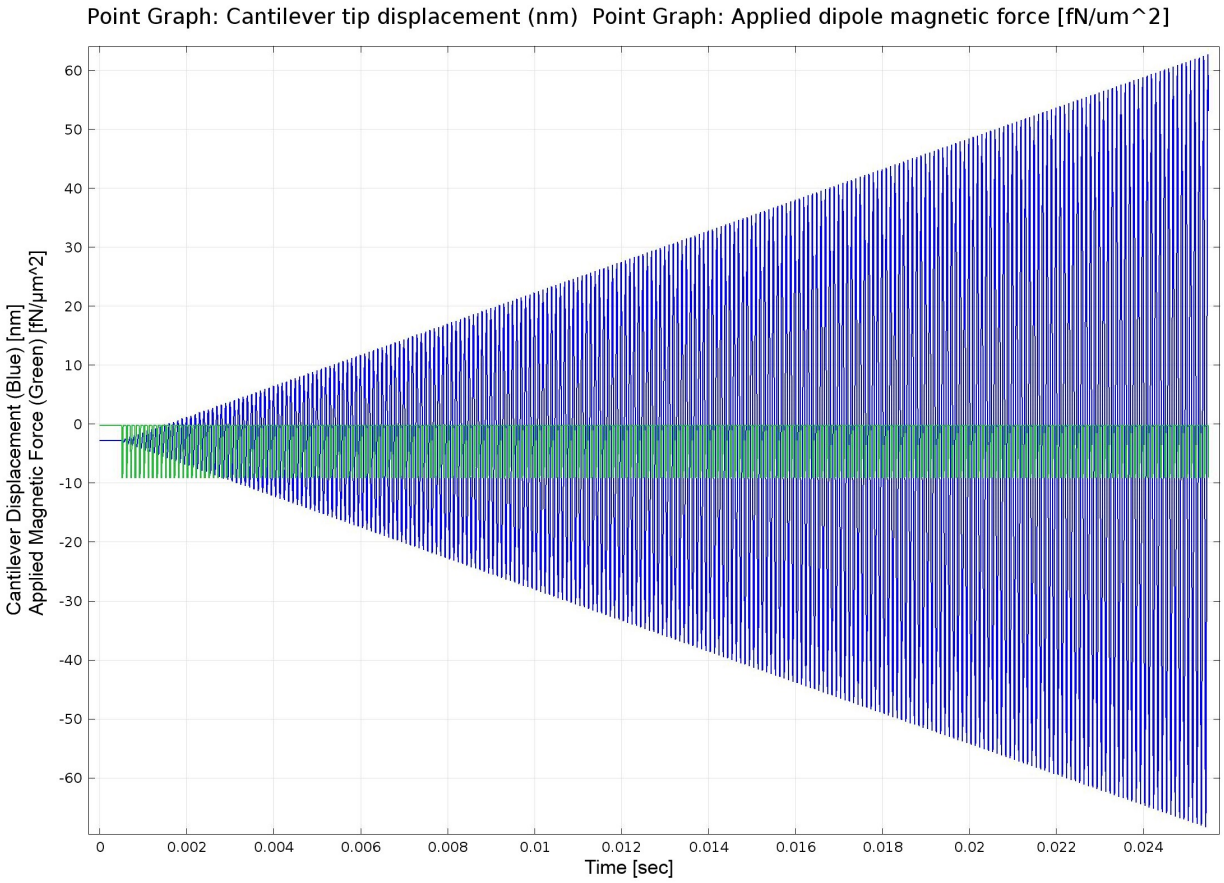

Figure 3.8: Cantilever deflection (blue) and applied dipole magnetic force (green) for the silicon nitride cantilever

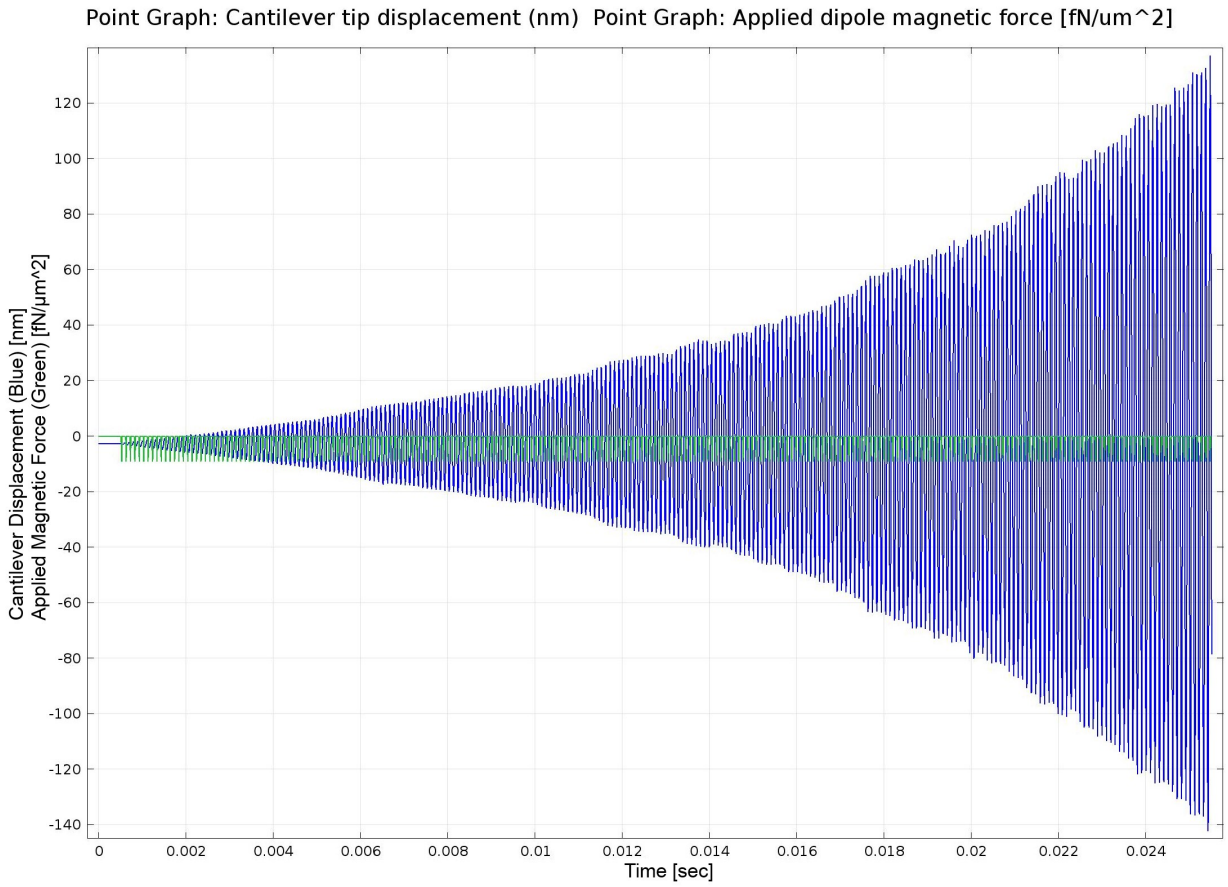

Figure 3.9: Cantilever deflection (blue) and applied dipole magnetic force (green) for the silicon cantilever

4. Sensor Design Considerations

This chapter will review the manufacturing consideration and procedure for the proposed mold spore sensor. It starts with the design criteria for the MEMS cantilever beam, permanent magnet and RF coil. This chapter will then discuss the supporting electronics and how they tie the components of the sensor together to detect the presence of a mold spore. The following section will discuss the manufacturing process of the proposed sensor and Section 4.7 defines the sequence of operation for the calibration and operation of the spore sensor. Figure 4.1 shows a simplified example of the proposed sensor arrangement without the magnets and RF coil, and Figure 4.2 shows the sensor in relation to the permanent magnets and RF coil.

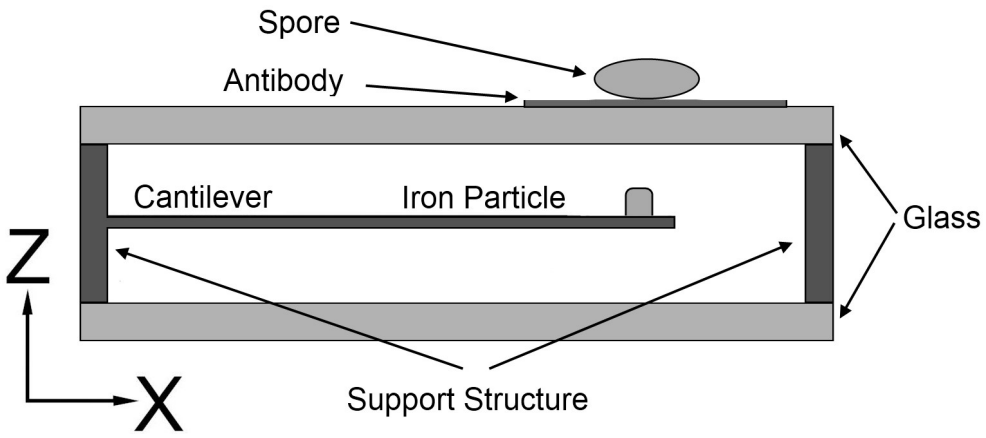

Figure 4.1: Simplified mold spore sensor setup

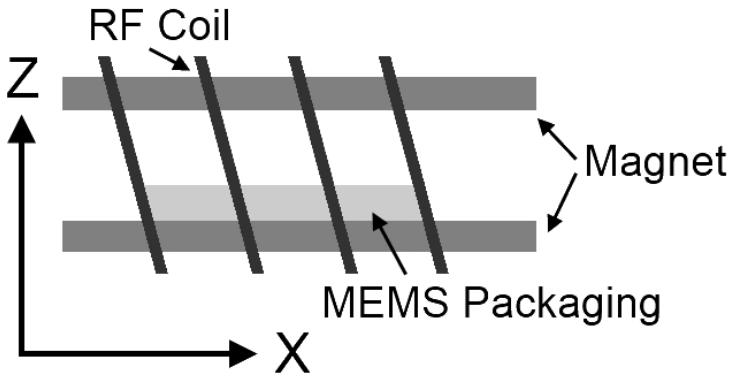

Figure 4.2: Proposed mold spore sensor with permanent magnet and RF coil.

4.1 MEMS Cantilever Design

Micro Electromechanical Systems are fabricated using a combination of photo lithography, CMOS fabrication techniques and material etching to create simple structures in materials such as silicon (amorphous, single crystal, doped, ect.), germanium and gallium arsenide. It is possible to introduce other metals and materials to the MEMS structure by including additional techniques such as sputtering and chemical vapor deposition to the fabrication process. Additional materials that can be added to a structure include iron, gold, titanium and silicon nitride.

As mentioned in the Chapter 2, for a typical MRFM setup the MEMS cantilever must possess a number of key characteristics such as a high quality factor (Q), a low spring constant, and an ideal natural resonance frequency between 10-15 kHz to help decouple the cantilever beam from vibrations outside the sensor [23]. The combination of these three characteristics reduces the minimum force detectable by the cantilever, as given in Eqn. 2.22. This section will be focusing on the silicon nitride cantilever discusses in Chapter 3.3 with the characteristics given in Table 3.4. The cantilever assembly has a collective mass of approximately 260 fg, a spring constant of 80.6×10^{-6} N/m and a natural resonance frequency of 10 kHz.

The paddle at the end of the cantilever serves two purposes. The first function is to act as a mounting point for the hemispherical iron particle with a radius of $1.5\mu m$. The

second purpose is to act as a reflective plane for the laser interferometer which measures the cantilever tip position during oscillations caused by the experiment.

4.2 Magnetic Materials

For the MRFM setup there are two magnetic systems that need to be considered. The first is the Ferromagnetic particle located in the center of the silicon paddle used to measure the change in the dipole magnetic force of the sample. The second magnetic system is the permanent magnet which is used to induce Zeeman splitting within the sample. The location and design of these magnetic systems greatly influences the overall operation of the sensor.

The ferromagnetic particle located on the paddle of the cantilever needs to be designed in such a way that there is enough iron to make the FM particle susceptible to minute changes in the dipole magnetic field of the sample without adding excessive mass to the cantilever. Eqn. 4.1 can be used to determine the number of atoms in the iron particle, where N_a is Avogadro's number ($6.022 \times 10^{23} \frac{1}{mol}$), the density, ρ, of Fe is 7.86 $\frac{g}{cm}$ and atomic mass, M_{at}, of 55.85 $\frac{kg}{mol}$ [8]. The iron particle used with a hemispherical shape and a radius of 1.5 μm has approximately 6×10^{11} atoms on which to act upon the induced dipole force, and has a mass of 55.6 fg.

$$\eta_{at} = \frac{\rho N_a}{M_{at}} \tag{4.1}$$

The design of the permanent magnet has a bit more leeway then the FM particle. It is possible to use a pair of large permanent magnets to provide a homogeneous magnetic field, β_{ext}, upon the sample. The magnets should be aligned such that the MEMS packaging and sample can be placed in the gap between the two magnets, as indicated in Figure 4.2. This configuration should provide a relatively homogeneous Zeeman splitting. For this design, it is desirable for the magnetic field strength between the two magnets to be a minimum of 0.5 Tesla, with an ideal strength of 0.9 Tesla. Ideally the magnetic field distribution between the two magnets should be less than 1 $\frac{T}{m}$ to provide a uniform magnetic field to the sample under test.

An alternative to the permanent magnet configuration mentioned above is the use of a

solid core electromagnet to provide the magnetic field. The advantage of using an electromagnet is that the field can be fine tuned to provide an optimal magnetic field strength. Care needs to be taken in the design of this electromagnet, as the magnetic field distribution needs to be as homogeneous as possible to prevent inconsistencies in the resonance signal.

4.3 RF Coil Design

The cantilever is designed such that the ratio between the applied RF frequency and the resonance frequency of the cantilever is greater than or equal to 10:1 which allows for the multiple cycles of the RF pulse to influence the net magnetization of the sample during a single oscillation of the cantilever [23]. For testing purposes, this design will be using a multi-turn RF coil made from copper wire located outside the MEMS packaging. This option has the advantage over MEMS based coils for this application including the ease of manufacturing and higher current carrying capacity of the larger copper wire to drive the RF pulse. With proper placement the RF coil can be aligned with the cantilever and the sample in such a way that the sample is located in the center of the coil loops, where the magnetization field of the RF pulse is maximum. Future considerations may include the adaptation of the coil design proposed by Zhang reviewed in Section 2.2.4 machined from a copper rod with a radius slightly larger then the final package size of the sensor. For this design, the RF coil is required to provide a magnetic field strength of approximately 300 μT.

4.4 Supporting Electronics

In addition to the magnetic resonance force microscopy setup described previously, there is a number of supporting electronic components which need to be incorporated into the final sensor packaging to provide accurate detection of spores. Such components include temperature and magnetic sensors to monitor the ambient conditions of the sensor. A laser interferometer focused on the cantilever such that the laser reflects off the cantilever paddle and onto an optical position sensor can be used to monitor the cantilever position and oscillation frequency. For this design, an optical position sensor with a minimum 1nm resolution is required to accurately trace the position of the cantilever beam during oscillation.

An embedded or external micro-controller is responsible for controlling the signal sent to the RF coil. The frequency of the RF signal passed to the coil is modulated based on the cantilever position, which is monitored by the micro-controller using the laser interferometer. The laser interferometer is also used for detecting the deflection of the cantilever during the harmonic oscillations caused by the spin flips of the sample during the MRFM experiment. The micro-controller will also have outputs for warning indicator LEDs which inform the operator of the status of the sensor and if it detects the presence of a mold spore. Since the most important signal of the sensor is the cantilever position given by the optical position sensor, its required that the micro-controller has an analog-to-digital converter (ADC) with a minimum of 10-bit resolution. Likewise the digital-to-analog converter (DAC) of the micro-controller should have a minimum resolution of 10-bits. The temperature and magnetic sensors do not require the same ADC requirements as the optical position sensor. In the event that the micro-controller is responsible to a number of spore sensors in an array, the temperature and magnetic sensors can be used for the entire array. Therefore the number of ADCs required by the micro-controller is $N + 2$ where N is the number of cantilever beams within the sensor. For example, the ATMEL SAM3S4C offers 15-10/12 bit ADCs and 2-12 bit DACs, which can support a 3 x 4 sensor array with one DAC and ADC remaining open for additional functionality. Figure 4.3 shows a functional description of the micro-controller and the supporting electronics and Section 4.7 breaks down the sequence of operation of the sensor.

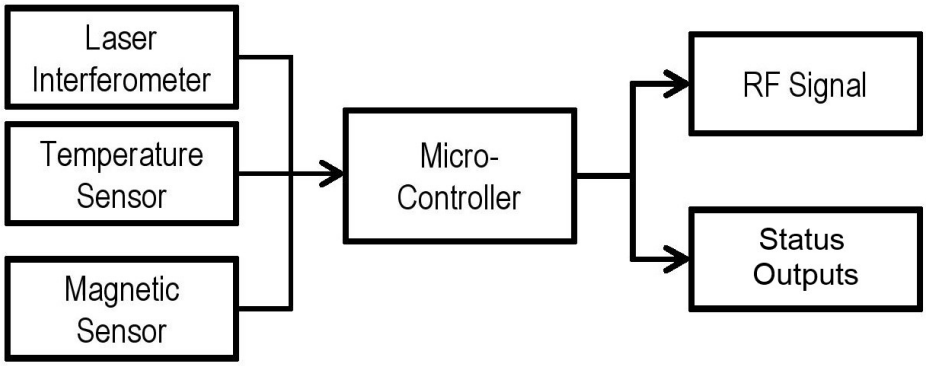

Figure 4.3: Micro-controller inputs and outputs.

4.5 Packaging Considerations

A number of considerations must be taken into account with the IC packaging of this mold spore sensor to prevent damage to the structure, maintain the operating environment of the cantilever and allow for an area which can be used as a sample slide where the spores can adhere to the monoclonal antibody with minimal damping of the magnetic force which acts between the cantilever and the sample.

The greatest packaging consideration is allowing the botrytis spores to adhere to the sensor within measuring range of the ferromagnetic particle and the magnetic field gradient which the iron tip produces. There are two methods which can be explored. The first method is to sandwich the cantilever structure between two plates of glass approximately 1 μm thick and located 3 μm above and below the cantilever beam. This approach can be completed under a fine vacuum, making it possible to seal the cantilever structure in the required 300 Pa operating pressure between the glass plates. By selectively coating the upper glass plate with a monoclonal antibody layer approximately 1 μm thick, it is possible to get the spore to adhere to the sensor packaging within 5 μm of the iron particle as simulated in Section 3.3.

The second method to get the spores within sensing range of the cantilever involves funneling the spores into the IC packaging, through an air pathway separated from the cantilever chamber and onto a thin sample slide within the IC. The downside to this approach is that the air containing the spores must be filtered to minimize contaminants which can plug the airways within the IC. The advantage of this configuration is that as long as the sample slide can be removed and replaced while maintaining the vacuum to the cantilever portion of the IC, then the exterior packaging can be made of a thicker and stronger material.

In order to maintain the operating environment of the cantilever beam, the MEMS packaging needs to be hermetically sealed to help maintain the low vacuum pressure of 300 Pa. The packaging may need to provide an external port to attach to a low vacuum displacement pump to maintain the vacuum in case of the hermetic seal failure, causing an increase in pressure. The hermetically sealed packaging also helps to lock out moisture that may con-

dense on the cantilever structure which can result in cantilever beam sticking to the lower or upper glass layers.

4.6 Manufacturing Process

While there are many different design considerations which may be examined to improve the sensing capability of the proposed sensor, a proof of concept sensor first needs to be manufactured and tested to verify operation. A number of steps are required in order to manufacture a prototype of the sensor. Starting with a silicon wafer $2\mu m$ thick, apply a positive tone resist such as polymethylmethacrylate (PMMA) and using an electron beam writerpattern a circle with a diameter of $3\mu m$ into the resist deep enough to reach the silicon wafer below. After developing the exposed resist in a Methylisobutylketone/Isopropanol (MIBK/IPA) solution then rinsed in isopropanol and dried, the result is a $3\mu m$ wide hole in the resist where the iron particle will be seated. A thin layer of Chromium/Gold alloy is evaporated onto the structure to act as a plating base which is then electroplated with iron until the hole is 75% filled.

Working in the $\langle 100 \rangle$ plane of the silicon wafer, the cantilever beam, paddle and supporting structure are next patterned into the PMMA and developed. A layer of silicon nitride approximately 200 nm thick is deposited on the exposed silicon using low-pressure chemical vapor deposition (LPCVD). The silicon nitride layer acts as a capping layer for the exposed iron particle, preventing corrosion during the remaining manufacturing process and the life of the sensor. After the deposition process, the remaining mask is stripped from the structure. Figure 4.4 presents the layout of the iron and silicon nitride development process and Figure 4.5 shows a proposed mask for cantilever patterning.

Placing the structure in a potassium hydroxide (KOH) bath, the exposed silicon is etched away while the deposited silicon nitride is not. As the KOH etches the wafer it will etch the silicon under the mask and will eventually free the silicon nitride cantilever beam from the silicon substrate. Since KOH causes anisotropic etching when used with silicon, the side wall profile of the surrounding support structure will be etched at an angle of 54.7° to the surface of the structure [32]. Figure 4.6 shows a cross section of the structure to show the

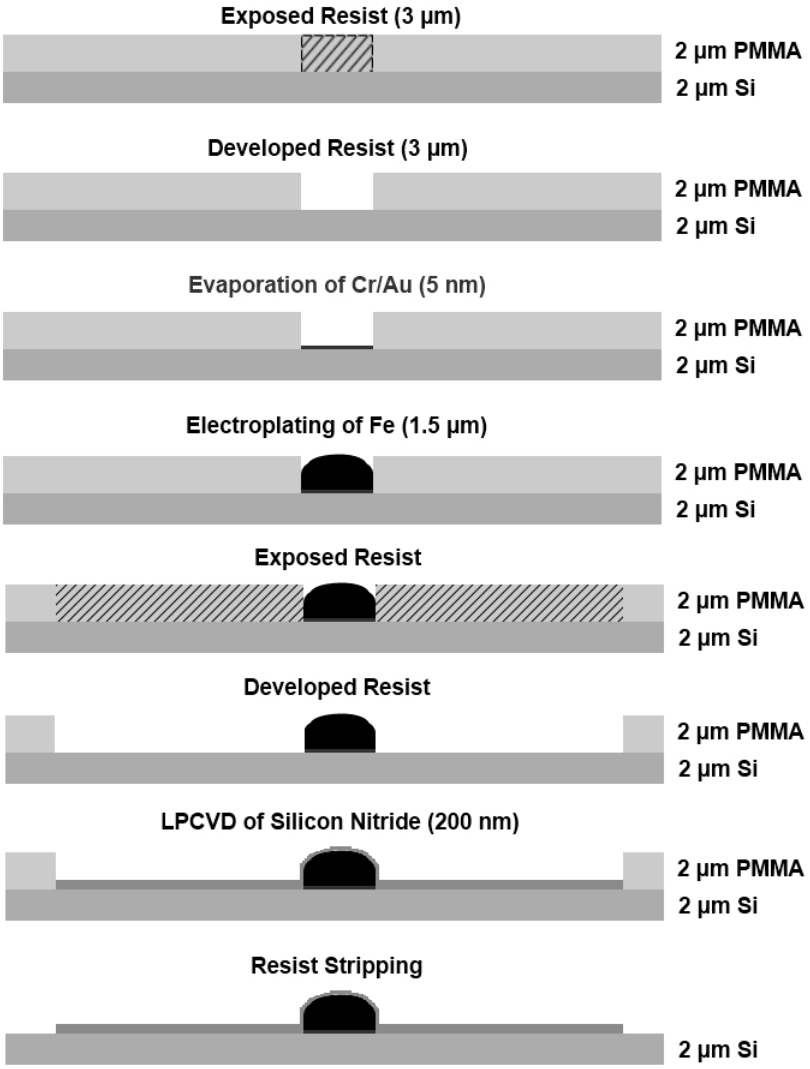

Figure 4.4: Cross section for process of depositing iron and silicon nitride to form cantilever paddle and iron particle assembly.

side wall profile of the support and the suspended silicon nitride cantilever.

The final etched structure can be sealed between thin glass wafers on silicon supports using either silicon fusion bonding or anodic (electrostatic) bonding under the 300 Pa vacuum conditions that the cantilever will operate in. The glass wafers act to protect the cantilever structure and maintain the vacuum within the structure. The top glass layer needs to be as thin as possible to maintain the vacuum without adding too much distance between the ferromagnetic particle and the sample, this glass layer will act as the sample slide which will

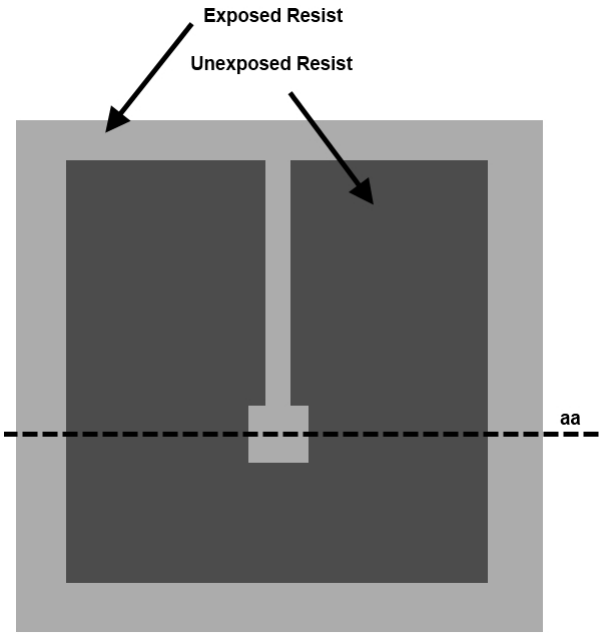

Figure 4.5: Mask used to develop cantilever and supporting structure. Exposed resist will be removed and exposed silicon coated with silicon nitride before resist is stripped and silicon is etched using KOH.

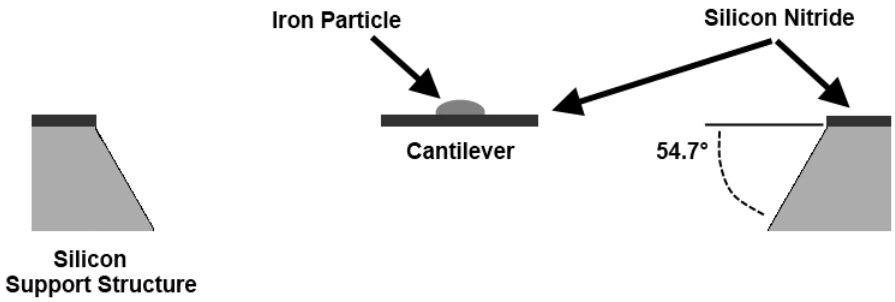

Figure 4.6: Cross section of freed silicon nitride cantilever and silicon support structure side wall profile along line 'aa' in Figure 4.5.

be coated with the monoclonal antibody. The lower glass layer does not need to be as thin as the upper layer but requires a pair of holes to be etched and fitted with the fiber optic cables needed for the laser interferometer before the bonding process. The top glass wafer of the sealed structure is then coated with a $1\mu m$ thick layer of the BC-12.CA4 monoclonal antibody above the iron tip to act as the binding interface of the sensor. A permanent

magnet can be placed directly below the lower glass wafer giving clearance room for the fiber optic cables as necessary.

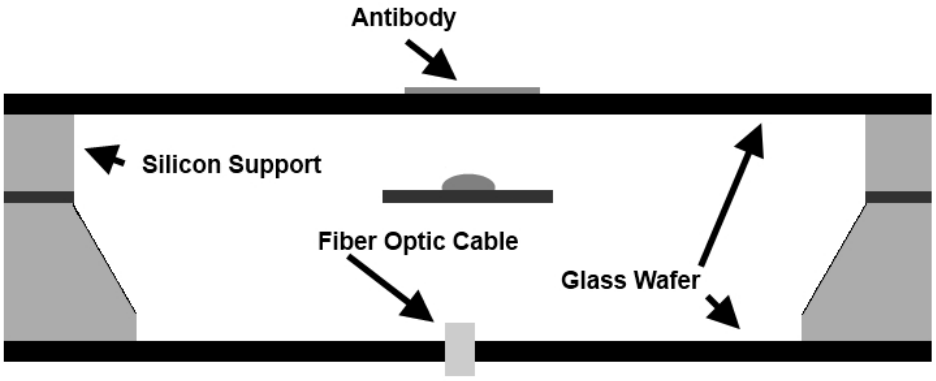

Figure 4.7: Cantilever structure sealed between glass wafers.

The entire assembly is then placed into a wire coil with an inner dimension of approximately $2mm$ such that the antibody layer is as close to the center of the coil as possible. Figure 4.7 shows a representation of the sealed MEMS structure and Figure 4.8 gives an idea of the final sensor with the coil and permanent magnet in place. The laser interferometer and RF coil are connected to the external micro-controller

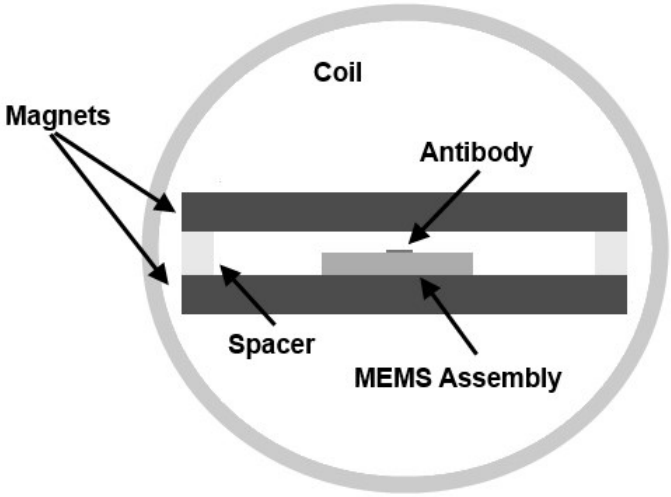

Figure 4.8: Sensor assembly with MEMS structure, permanent magnet and RF coil.

4.7 Sequence of Operation

As mentioned in Section 4.4, a micro-controller is responsible for the operation of the proposed mold spore sensor. Numerous steps need to be taken in order for the micro-controller to properly control the RF signal and monitor the cantilever response in order to detect the presence of a mold spore. Because the MEMS manufacturing process is not flawless, minute imperfections in the MEMS cantilever or the iron particle geometry can cause the resonance frequency of the cantilever beam to shift to a higher or lower frequency. Since each cantilever structure is slightly different the controller needs to be calibrated to the sensor setup before it can reliably begin the spore detection process.

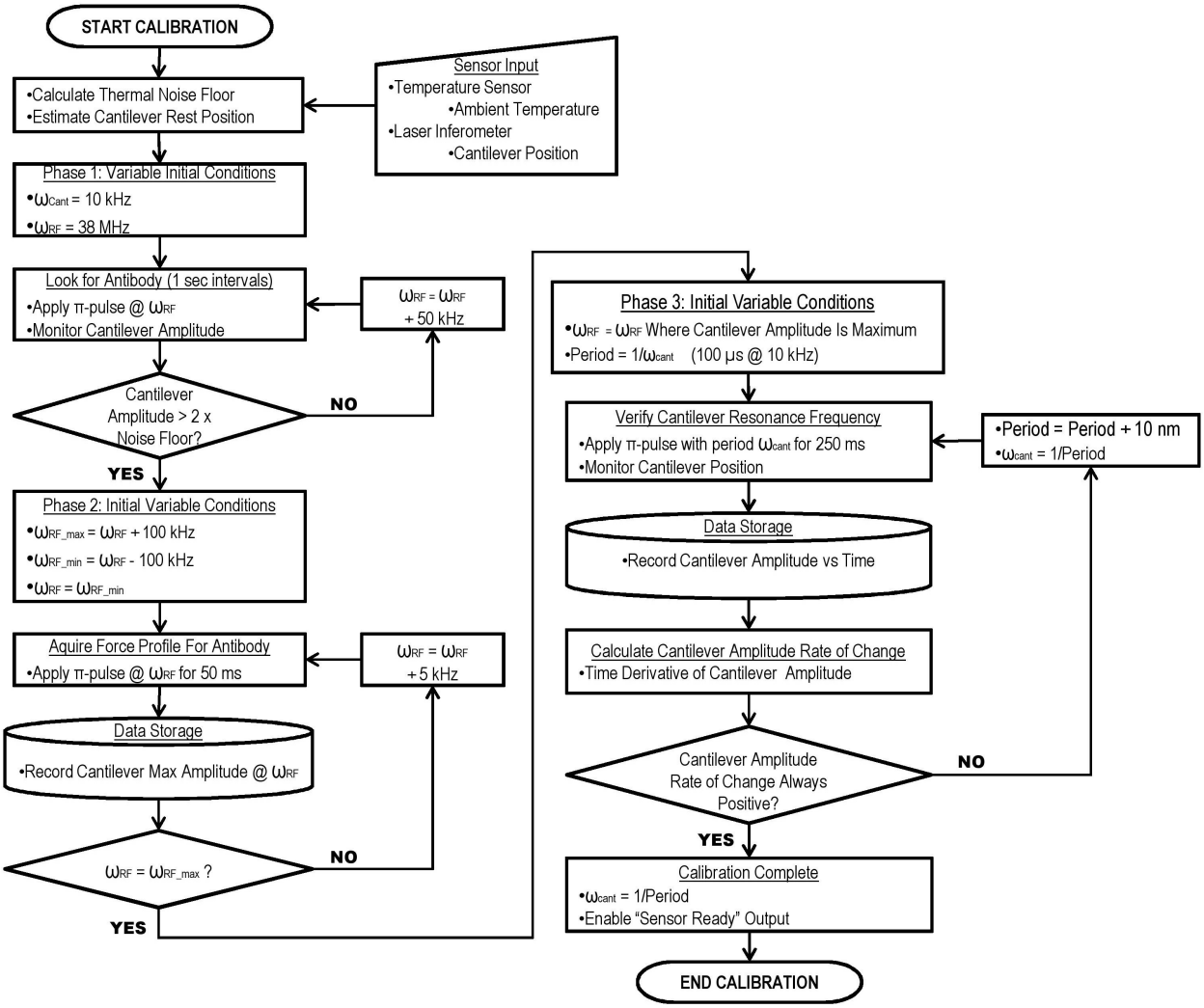

Figure 4.9: Flowchart for sensor calibration routine

The calibration begins by using the temperature sensor and laser interferometer to measure the oscillation amplitude of the cantilever due to thermal vibrations, this value will be noted as the noise floor for the current temperature. This process may be repeated at different ambient temperatures so that the micro-controller can account for the change in thermal vibrations over a span of temperatures. The cantilever beam is physically isolated from the outside environment and has a resonance frequency of 10 kHz, environmental influences such as wind, ran and motor vibrations should be minimized and not considered in this work. The stationary position of the cantilever beam can be estimated by averaging the amplitude of the thermal vibrations over time. For the next step, the micro-controller will assume that the cantilever resonance frequency is 10 kHz and begin to apply a series of the π-pulse sequence described in Section 2.2.5 to the RF coil at approximately 38 MHz in an attempt to induce a resonance slice within the BC-12.CA4 antibody. The cantilever oscillation is monitored and if a change in amplitude is detected after an arbitrary time, then the controller can assume that some portion of the resonance slice is currently in the antibody. If the cantilever oscillation does not change significantly during the applied RF sequence, then the controller shifts the RF frequency in 50-100 kHz increments and attempts the test again. Once the antibody has been located by the controller the RF pulse is shifted in increments of 5-10 kHz until the frequency which produces the maximum force is located. The maximum force will be found when the apex of the paraboloid shaped resonance slice is located within the antibody layer; where the number of spins is maximized.

Using the RF frequency which results in the maximum force from the antibody, the controller will continue to apply a series of π-pulses while adjusting the period between the pulses in 10 ns increments. The interferometer is used to monitor cantilever oscillations as the period is adjusted; the micro-controller calculates the rate that the cantilever amplitude changes until a maximum change rate is found. At this point the period between pulses is approximately the same as the period of the cantilever oscillation; from this information the controller can calculate the actual resonance frequency of the cantilever. Figure 4.9 shows the flowchart used for the calibration sequence of the sensor micro-controller.

Once the calibration has been finished the controller will enable a “sensor ready” output,

which can be connected to a status LED or to a more complex system (such as an alarm or building management system) to indicate that the sensor is ready to begin detection. The calibration process can be repeated once every day or two to ensure that the readings from the sensor haven't drifted from the original calibration. During the detection process the micro-controller sends a 38.4 MHz π-pulse to the RF coil in 10 ms bursts and measures the deflection of the cantilever using the laser interferometer. From Figure 3.7 a frequency of 38.4 MHz should result in the apex of the resonance slice located appropriately 3 μm above the antibody layer. In the absence of a mold spore adhered to the antibody coating of the sensor there should be no measurable change in oscillation of the cantilever beam during the π-pulse burst. However if a mold spore is adhered to the sensor then the change in the cantilever oscillation amplitude should be detectable, at this point a high resolution scan of the sample is performed to determine if there is a spore present or some unknown particle has contaminated the sensor by comparing lab profiles of the spore to the profile built from the sample.

If a spore is suspected to be present by the micro-controller the sensor will begin a high resolution scan of the sample for confirmation. Using a series of π-pulses sweeping between 38.2 MHz and 38.8 MHz and monitoring the cantilever oscillation amplitude, the controller can devise a frequency-force profile for the sample. Once the high resolution scan is complete, the frequency-force profile can be compared to stored profiles of the spore. If the two spore profiles match each other within a given tolerance, the controller will enable a status output to indicate that a spore has been found. If the frequency-force profiles do not match within the given tolerance, the controller will enable a status output to indicate that a foreign substance has contaminated the sensor. Figure 4.10 gives the proposed detection sequence for the sensor.

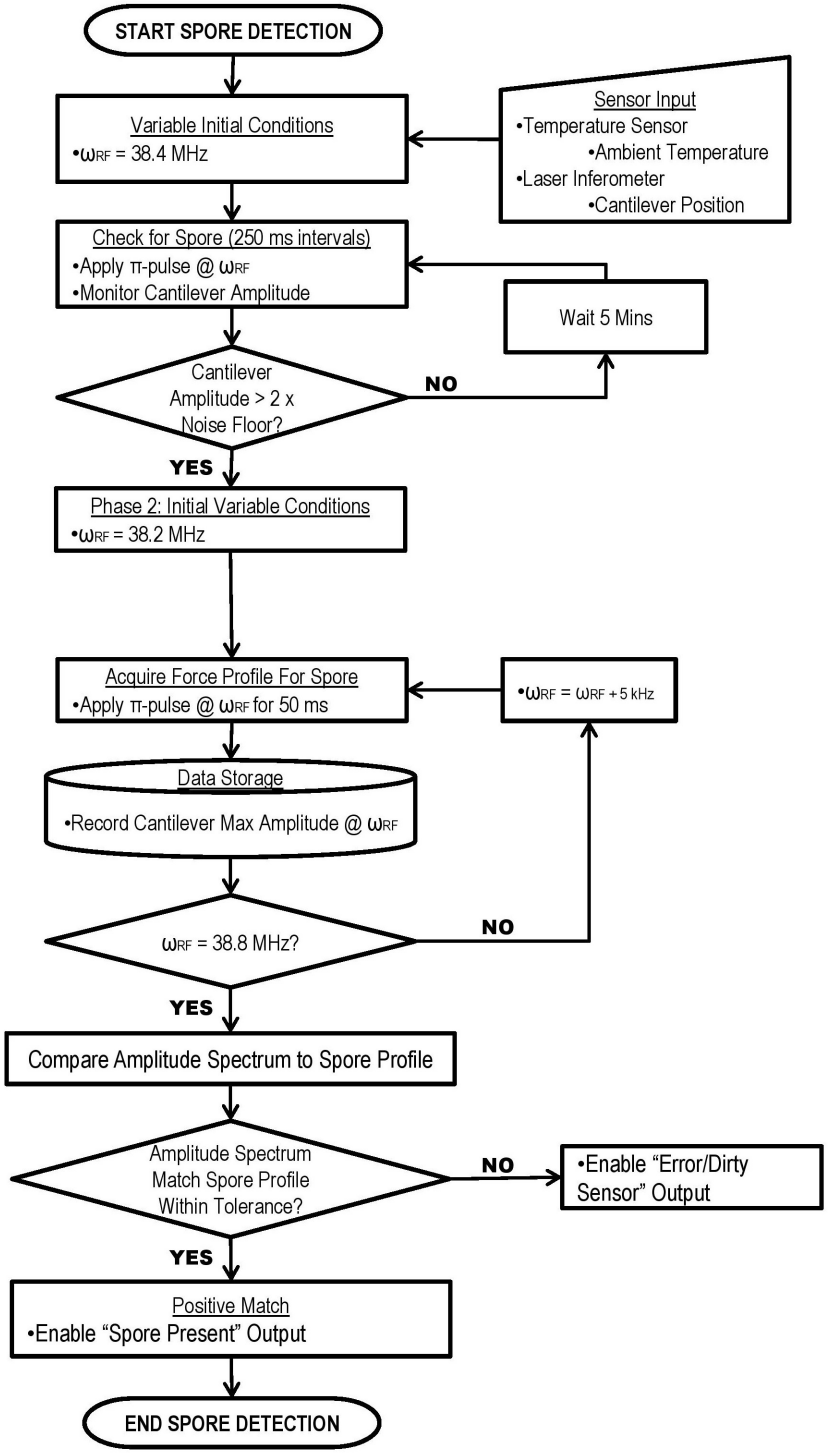

Figure 4.10: Flowchart for fungal spore detection routine.

5. Conclusion

5.1 Summary

This work explores the feasibility of using magnetic resonance force microscopy for use in the detection of the botrytis cinerea mold spore. Two cantilever models using different materials were designed and revised in order to maximize the mechanical quality factor of the cantilever beam operating at the low vacuum pressure of 300 Pa and an ambient temperature up to 300°K. The silicon cantilever has dimensions of $110.3\mu m \times 2\mu m \times 200nm$, a spring constant of 79.1×10^{-6} N/m and a quality factor of 28.7. The silicon nitride cantilever has the dimensions of $114.8\mu m \times 2\mu m \times 200nm$, a spring constant of 80.6×10^{-6} N/m and has a quality factor of 30.0.

MRFM simulations were performed on a homogeneous blank the same shape and size of the botrytis spore with a hydrogen spin density of 9.4 $\frac{Spins}{100nm^3}$. The blank was located $5\mu m$ from the cantilever tip at rest and resulted in a maximum force of 340 fN at 38.372 MHz and a detectable force between 38.29 MHz and 38.60 MHz. Using the π-pulse method to induce spin flips in the magnetic moment of the ^1H spin, it was determined that it would take approximately 5 ms for the silicon cantilever to reach a harmonic oscillation with an amplitude twice that of the thermal vibrations of the cantilever. For the silicon nitride cantilever, harmonic oscillations which doubled the amplitude of the thermal vibrations obtained after an estimated 4 ms.

Section 4 discusses the manufacturing process for the proposed sensor and addresses a number of additional design considerations which can be incorporated in future sensor revisions. The role of supporting electronics such as the micro-controller and various sensors were also discussed in the overall sensor design. The tentative sequence of operation for the

calibration and operation of the spore sensor were also discussed in Section 4.

5.2 Conclusion

The sensor proposed and simulated in this work shows that using magnetic resonance force microscopy is a feasible solution for the detection of a single mold spore. By integrating this sensor in existing spore traps, it is possible to quickly identify the presence of airborne botrytis cinerea spores without the need for filter transportation and identification by trained technicians. This unique design can be modified relatively easily for the detection of additional spore types by changing the antibody used to another monoclonal or polyclonal antibody and devising a profile for the target spore. By using magnetic resonance force microscopy with large frequency steps, the sensor is able to verify the presence of a mold spore adhered to the antibody coating, then smaller frequency steps are used to develop a deflection-frequency profile to positively identify the spore type adhered to the sensor. Since the size of the MEMS portion of the sensor is extremely small, it is quite possible that an array of cantilever beams can be used to increase the size of the spore contact surface. By incorporating different antibodies into the sensor array it is possible to design a sensor capable of detecting multiple species of fungal spores simultaneously.

Section 1.2 detailed the research objectives for this thesis. The first objective was to estimate the magnetic force during a MRFM experiment on a sample the size of the botrytis cinerea spore, this force is required to drive the cantilever oscillations and is maximum when the applied RF pulse is at a given frequency. Chapter 3 discusses the MATLAB scripts used to estimate the dipole magnetic force which results from a botrytis shaped sample. The results of this simulation show that when the cantilever tip is 4 μm from the sample the maximum dipole magnetic force is estimated at 480 fN when an RF pulse of 38.35 MHz is applied. When the distance between the sample and the cantilever tip is increased to 6 μm the maximum force is deceased to 230 fN at a frequency of 38.39 MHz. As the cantilever beam oscillates, the magnetic force will vary at a rate of 0.1257 fN/nm and the RF pulse will need to change at a rate of 16 Hz/nm in order to maintain the position of the resonance slice.

The second research objective was to estimate the cantilever beam dimensions in order to minimize the spring constant of the beam. A low spring constant is desirable because it increases the cantilever sensitivity to minute changes in the net magnetization of the sample under test. The MATLAB script used to estimate the cantilever dimensions estimated that a silicon cantilever of size $116.7\mu m \times 2.12\mu m \times 200nm$ and a silicon nitride cantilever of dimensions $119.5\mu m \times 2.17\mu m \times 200nm$ would result in spring constants of 454×10^{-6} and 636×10^{-6}. These cantilever sizes were entered into COMSOL Multiphysics and revised such that the cantilever dimensions are $107.1\mu m \times 2.0\mu m \times 200nm$ and $114.8\mu m \times 2.0\mu m \times 200nm$ for silicon and silicon nitride cantilevers respectively with spring constants approximately 80×10^{-6} each.

The third objective outlines in Section 1.2 was to estimate the time required for driven cantilever oscillations to overcome the noise floor of the sensor and be distinguishable from the thermal vibrations of the cantilever beam. For the silicon cantilever beam outlined above the estimated thermal vibration amplitude is 5nm, for an applied harmonic force of 100 fN, the driven cantilever oscillations reached an amplitude of 10nm in 4ms and an amplitude of 60nm in 22ms. For the silicon nitride cantilever the thermal vibrations are estimated at 4nm, the driven cantilever oscillations reach an amplitude of 8nm in 5ms and a 60nm amplitude in 18ms.

One of the major drawbacks for using MRFM as a detection device for mold spores is that the magnetic resonance force microscopy is sensitive to the temperature of the sensor. In an environment with a high ambient temperature, the Boltzmann distribution given in Eqn. 2.5a indicates that the ratio of α and β spins is extremely close to 1:1 and limits the number of spins that can transition between the α and β states. However if the sensor is located in a low temperature environment, the number of spins which can transition between the α and β states increases, which will result in a larger force to act on the iron particle.

The sensor proposed in this work was designed in such a way that the cantilever beam is isolated from external environmental conditions such as wind and rain. With a resonance frequency of 10 kHz, the cantilever beam should be relatively isolated from nearby mechanical vibrations. However the simulations performed are unable to take into account how the

sensor will react if contaminants such as dust, rain droplets or insects get caught in the sensing range of the iron particle during a MRFM scan. Additional research into how the sensor responds to foreign contamination needs to be done. Additional research needs to be done in regards to the BC-12.CA4 antibody to determine if external environmental conditions can influence the bonding mechanism of the sensor, as this property may influence the lifetime of the sensor.

5.3 Future Work

Even though the simulations on the mold spore sensor are complete and the design proven to be feasible, there are still a number of tasks that need to be performed before the sensor can be manufactured on a large scale. The first step is to build a prototype of the sensor to verify the operational characteristics of the cantilever beam including resonance frequency and quality factor. Once these parameters have been verified and the micro-controller has been calibrated, a single botrytis cinerea spore will need to be placed on the antibody coating of the sensor and a high resolution scan of the spore will need to be run to obtain a deflection-frequency profile for the spore. Additional spores at different orientations will need to be profiled as well so that in the field the sensor will have a higher probability of positively identifying a randomly oriented spore.

Once the sensor has been manufactured and tested, additional modification can be considered to improve the performance of the proposed sensor. One such improvement includes attempting to detect other dipolar isotopes, such as ^{13}C, within the sample to provide additional features for the spore identification process. Another consideration for potentiality improving the spore sensor is to adopt the modified Alderman-Grant coil proposed by Zhang and discussed in Section 2.2.4. Once the design of a single sensor has been thoroughly tested, an array of mold spore sensor can be fabricated to increase the contact surface of the sensor design or to detect other spores which may be on interest.

References

[1] S. L. Jackson and K. L. Bayliss, "Spore traps need improvement to fulfill plant biosecurity requirements," *Plant Pathology*, vol. 60, pp. 801–810, Oct. 2011.

[2] R. C. Calhelha, J. V. Andrade, I. C. Ferreira, and L. M. Estevinho, "Toxicity effects of fungicide residues on the wine-producing process," *Food Microbiology*, vol. 24, no. 4, pp. 393–398, 2006.

[3] T. D. Stowe, K. Yasumura, T. W. Kenny, D. Botkin, K. Wago, and D. Rugar, "Attonewton force detection using ultrathin silicon cantilevers," *Applied Physics Letters*, vol. 71, no. 2, pp. 288–290, 1997.

[4] G. P. Berman, F. Borgonovi, V. N. Gorshkiv, and V. I. Tsifrinovich, *Magnetic Resonance Force Microscopy and a Single-Spin Measurement*. World Scientific Publishing Co., 2006.

[5] C. Degen, M.Poggio, C. Rettner, and D. Rugar, "Nanoscale magnetic resonance imaging," *Proceedings of National Academy of Sciences of the United States of America*, vol. 106, pp. 1313–1317, Feb. 2009.

[6] M. K. Tan and D. Wright, "Enhancing the detection of tilletia indica, the cause of karnal bunt - final report," p. 63, 06/2009 2009.

[7] T. L. Brasel, J. M. Martin, C. G. Carriker, S. C. Wilson, and D. C. Straus, "Detection of airborne stachybotrys chartarum macrocyclic trichothecene mycotoxins in the indoor environment," *Applied and Enviromental Microbiology*, vol. 71, pp. 7376–7388, Nov. 2005.

[8] S. Kasap, *Principles of Electrical Engineering Materials and Devices*. McGraw Hill, 2000.

[9] J. H. Nelson, *Nuclear Magnetic Resonance Spectroscopy*. Prentice Hall, 2003.

[10] Michigan State University - Department of Chemistry, "Nuclear magnetic resonance spectroscopy." http://www2.chemistry.msu.edu/faculty/reusch/VirtTxtJml/Spectrpy/nmr/nmr1.htm. Accessed: 12/02/2011.

[11] M. Nerz-Stormes, "The basics nuclear magnetic resonance spectroscopy." http://www.brynmawr.edu/chemistry/Chem/mnerzsto/The_Basics_Nuclear_Magnetic_Resonance_Spectroscopy_2.htm. Accessed: 08/05/2012.

[12] A. Carrington and A. D. McLachlan, *Introduction to Magnetic Resonance with Applications to Chemistry and Chemical Physics*. Harper and Row, 1967.

[13] M. J. Duer, *Introduction to Solid-State NMR Spectroscopy*. Blackwell Publishing Ltd, 2004.

[14] H. Assumption, J. Vermeulen, W. Jarrett, L. Mathias, and A. van Reenen, "High resolution solution and solid state nmr characterization of ethylene/1-butene and ethylene/1-hexene copolymers fractionated by preparative temperature rising elution fractionation," *Polymer*, vol. 47, no. 1, pp. 67 – 74, 2006.

[15] W.-C. Lin and G. Fedder, "A comparison of induction-detection nmr and force-detection nmr on micro-nmr device design," Tech. Rep. CMU-RI-TR-01-06, Robotics Institute, Pittsburgh, PA, March 2001.

[16] K. Y. Yasumura, T. D. Stowe, W. M. Chow, T. Pfafman, T. Kenny, B. Stipe, and D. Rugar, "Quality factors in micron- and submicron-thick cantilevers," *Journal of Microelectromechanical Systems*, vol. 9, no. 1, pp. 117–125, 2000.

[17] J. Brotz, *Damping in CMOS-MEMS Resonators*. PhD thesis, Carnegie Mellon University, Pittsburgh, Pennsylvania, United States of America, 2004.

[18] T.-R. Hsu, *MEMS and Microsystems: Design, Manufacture, and Nanoscale Engineering*. John Wiley and Sons Inc., 2008.

[19] K. Naeli and O. Brand, "Dimensional considerations in achieving large quality factors for resonant silicon cantilevers in air," *Journal of Applied Physics*, vol. 105, no. 1, p. 014908, 2009.

[20] J. A. Pelesko and D. H. Bernstein, *Modeling MEMS and NEMS*. Chapman Hall, 2003.

[21] C. Zener, "Internal friction in solids. I. Theory of internal friction in reeds," *Phys. Rev.*, vol. 52, pp. 230–235, Aug 1937.

[22] C. Zener, "Internal friction in solids II. General theory of thermoelastic internal friction," *Phys. Rev.*, vol. 53, pp. 90–99, Jan 1938.

[23] M. D. Chabot, J. M. Moreland, L. Gao, S.-H. Liou, and C. W. Miller, "Novel fabrication of micromechanical oscillators with nanoscale sensitivity at room temperature," *Journal of Microelectromechanical Systems*, vol. 15, pp. 1118–1126, Oct. 2005.

[24] G. P. Berman and V. I. Tsifrinovich, "Modified approach to single-spin detection using magnetic resonance force microscopy," *The American Physical Society*, vol. 61, pp. 3524–3527, Feb. 2000.

[25] Z. Zhang, P. C. Hammel, and G. J. Moore, "Application of a novel rf coil design to the magnetic resonance force microscope," *Review of Scientific Instruments*, vol. 67, no. 9, pp. 3307–3309, 1996.

[26] M. Choquer, E. Fournier, C. Kunz, C. Levis, J.-M. Pradier, A. Simon, and M. Viaud, "Botrytis cinerea virulence factors: new insights into a necrotrophic and polyphageous pathogen," *FEMS Microbiology Letters*, vol. 277, pp. 1–10, Oct. 2007.

[27] T. Prins, P. Tudzynski, A. V. Tiedemann, B. Tudzynski, A. T. Have, M. Hansen, K. Tenberge, and J. V. Kan, "Infection strategies of botrytis cinerea and related necrotrophic pathogens," in *Fungal Pathology*, pp. 33–64, Kluwer Academic Publishers, 2000.

[28] M. B. Ellis and J. M. Waller, "Sclerotinia fuckeliana (conidial state: Botrytis cinerea)," *CMI descriptions of pathogenic fungi and bacteria*, vol. 431, pp. 7376–7388, 1974.

[29] J. W. Kimball, *Introduction to Immunology*. Macmillan Publishing Company, 3 ed., 1990.

[30] A. Mohr, *Use of monoclonal antibody to detect grat mold (Botrytis cinerea) in strawberry*. PhD thesis, McGill University, 2001.

[31] M. R. Churchill, "Carbon-hydrogen and nitrogen-hydrogen distances assumed in, and determined from, recent x-ray diffraction studies on inorganic complexes," *Inorganic Chemistry*, vol. 12, no. 5, pp. 1213–1214, 1973.

[32] S. Beeby, G. Ensell, M. Kraft, and N. White, *MEMS Mechanical Sensors*. Artech House, Inc., 2004.